

Uniform volumetric single-cell processing for organ-scale molecular phenotyping

Received: 15 May 2019

Accepted: 11 December 2024

Published online: 24 January 2025

 Check for updates

Dae Hee Yun ^{1,2,7}, Young-Gyun Park^{2,3,7}, Jae Hun Cho⁴, Lee Kamensky^{2,3}, Nicholas B. Evans^{2,3}, Nicholas DiNapoli^{2,3}, Katherine Xie^{2,3}, Seo Woo Choi^{2,4}, Alexandre Albanese^{2,3}, Yuxuan Tian⁴, Chang Ho Sohn ^{2,3}, Qiangge Zhang^{1,5,6}, Minyoung E. Kim ^{1,2}, Justin Swaney⁴, Webster Guan⁴, Juhyuk Park^{2,3,4}, Gabi Drummond¹, Heejin Choi^{2,3}, Luzdary Ruelas⁴, Guoping Feng ^{1,5,6} & Kwanghun Chung ^{1,2,3,4,6} 

Extending single-cell analysis to intact tissues while maintaining organ-scale spatial information poses a major challenge due to unequal chemical processing of densely packed cells. Here we introduce Continuous Redispersion of Volumetric Equilibrium (CuRVE) in nanoporous matrices, a framework to address this challenge. CuRVE ensures uniform processing of all cells in organ-scale tissues by perpetually maintaining dynamic equilibrium of the tissue's gradually shifting chemical environment. The tissue chemical reaction environment changes at a continuous, slow rate, allowing redispersion of unevenly distributed chemicals and preserving chemical equilibrium tissue wide at any given moment. We implemented CuRVE to immunologically label whole mouse and rat brains and marmoset and human tissue blocks within 1 day. We discovered highly variable regionalized reduction of parvalbumin immunoreactive cells in wild-type adult mice, a phenotype missed by the commonly used genetic labeling. We envision that our platform will advance volumetric single-cell processing and analysis, facilitating comprehensive single-cell level investigations within their spatial context in organ-scale tissues.

In recent years, the field of single-cell analysis has revolutionized understanding of cellular heterogeneity and functional diversity within tissues. Scalable and automated technologies, such as flow cytometry and single-cell RNA sequencing, have provided insights into complex biological processes by enabling the quantitative analysis of biological systems at single-cell resolution and providing detailed information on cell populations and gene expression relationships^{1,2}. Integration of such data with immunohistochemistry, *in situ* hybridization and spatial transcriptomics can investigate genetic spatial context^{3–5}, epigenetic

modifications^{6,7}, translational abundance⁸ and post-translational modifications⁹.

Single-cell analysis methods necessitate a series of multi-step chemical processing, such as fixation, labeling and washing. Uniform chemical treatment of all cells is pivotal to attain accurate, quantitative and comparable single-cell readouts. Conventionally, uniform treatment of cells has been achieved through tissue dissociation into suspended cells or dissection of tissue into ultra-thin sections to facilitate direct exposure of all cells to a thoroughly mixed chemical environment¹⁰.

¹Department of Brain and Cognitive Sciences, Massachusetts Institute of Technology (MIT), Cambridge, MA, USA. ²Picower Institute for Learning and Memory, Massachusetts Institute of Technology (MIT), Cambridge, MA, USA. ³Institute for Medical Engineering and Science, Massachusetts Institute of Technology (MIT), Cambridge, MA, USA. ⁴Department of Chemical Engineering, Massachusetts Institute of Technology (MIT), Cambridge, MA, USA. ⁵Yang Tan Collective and McGovern Institute for Brain Research, Massachusetts Institute of Technology (MIT), Cambridge, MA, USA. ⁶Stanley Center for Psychiatric Research, Broad Institute of MIT and Harvard, Cambridge, MA, USA. ⁷These authors contributed equally: Dae Hee Yun, Young-Gyun Park.  e-mail: khchung@mit.edu

Volumetric intact tissue processing and imaging is a promising approach to achieve organ-scale single-cell analysis while accurately capturing spatial contexts as well as connectivity information. Innovations in tissue clearing and tissue engineering technologies have enabled transformation of tissue into a transparent macromolecule-permeable hydrogel^{11–14}. Methodologies to achieve holistic labeling of whole organs via transgenic¹⁵ or molecular labeling approach^{16–32} are also advancing rapidly. Combined with the rapidly evolving field of lightsheet microscopy³³ and artificial intelligence (AI)-driven analysis, whole intact organs can now be imaged and analyzed at cellular and subcellular resolution.

Despite its potential, the transition of true single-cell analysis from one-dimensional (1D) (dissociated single cells) and two-dimensional (2D) (ultra-thin tissue sections) to three-dimensional (3D) organ-scale tissues still poses a formidable challenge. In intact mammalian organs (for example, mouse brain), tens of millions of cells are densely packed. Even with improved permeabilization through tissue transformation, dense intact organs impede the efficient transport of necessary chemicals essential for single-cell analysis from the organ surface to its core. Only cells near the organ surface are directly exposed to a thoroughly mixed chemical environment. Consequently, cells located in different parts of the organ experience unequal chemical processing, creating disparities that compromise the comparability of obtained results. This issue mirrors the challenge encountered when attempting to merge results from differently processed batches of dissociated cells for data integration¹.

To address this fundamental challenge of volumetric single-cell processing and analysis, we introduce Continuous Redispersion of Volumetric Equilibrium (CuRVE) in nanoporous matrices. Unequal processing of cells in organ-scale tissue occurs because the chemical environment surrounding cells is spatially disturbed due to various factors, such as slow chemical transport and rapid chemical reactions throughout the tissue (Fig. 1a). We hypothesized that, if such spatial disturbance in chemical environment can be eliminated, perfectly uniform processing of all cells in volumetric tissues would be possible. With CuRVE, the change in tissue chemical reaction environment occurs at a continuous rate slow enough to allow the redispersion of unevenly distributed chemicals, maintaining chemical equilibrium tissue wide at any given moment. By perpetually maintaining a dynamic equilibrium state, the entire system can undergo uniform chemical composition changes necessary for cell processing, ensuring that all cells in intact tissues consistently experience the same processing conditions (Fig. 1b).

To demonstrate the value of implementing CuRVE, we focused on its implementation in organ-scale intact tissue immunolabeling, which is a challenging step in tissue processing and high-resolution organ-scale imaging. Immunolabeling benefits from the specificity and robustness of immunoglobulins as molecular probes; however, their slow tissue penetration and high reactivity create disparate antibody concentrations throughout the tissue volume, causing unequal chemical processing of cells and uneven labeling. The large difference between slow transport rate and fast reaction rate, along with the heterogeneous properties of both protein targets and probes, presents challenges to develop a practical one-size-fits-all solution. Extensive research has been done to shift the reaction–diffusion balance to facilitate deep immunolabeling, including system-wide reaction inactivation and subsequent reactivation (the SWITCH concept¹⁹), partial reaction inhibition via specialized buffer formulation (CUBIC-HistoVision¹⁷) and partial reaction inhibition using high temperature (ThICK/SPEARs²¹). These methods have convincingly demonstrated organ-scale immunolabeling; however, realizing CuRVE will be able to more efficiently and uniformly process intact tissues in more versatile applications.

We also present electrophoretic-Fast Labeling using Affinity Sweeping in Hydrogel (eFLASH) as a proof of concept for CuRVE implementation in intact tissue immunolabeling. In eFLASH, we gradually

change the tissue-wide chemical environment (for example, buffer composition and antibody concentration) from inhibition of antibody binding to normal binding while maintaining tissue-wide chemical equilibrium at any given moment. In this process, electrophoretically enhanced chemical transport rapidly disperses chemicals to minimize the spatial discrepancy of chemical compositions and quickly re-establish tissue-wide equilibrium.

We first conducted computational simulation to theoretically demonstrate that CuRVE can enable superior organ-scale uniform processing of cells. Then, to implement CuRVE for volumetric immunolabeling, we devised a dual sweeping of antibody binding modulators (pH and deoxycholic acid) for broadly compatible regulation of antibody reaction strength. The resulting technology that we named eFLASH achieved rapid and uniform immunolabeling of intact tissue within just 1 day for mouse organs, rat brains as well as marmoset and human tissues blocks. Using eFLASH, we discovered large-scale regionalized reduction of parvalbumin immunoreactive (PV⁺) cells in healthy wild-type mice with individual and cross-hemisphere variabilities. Finally, we applied eFLASH to perform a comparative analysis between transgenic and immunological labeling that revealed discrepancies between PV-Cre/*loxP*-tdTomato double transgenic reporter line and immunological labeling of PV⁺ cells, establishing the importance of scalable volumetric immunolabeling for characterization of baseline proteomic expression, individual variabilities and pathological changes.

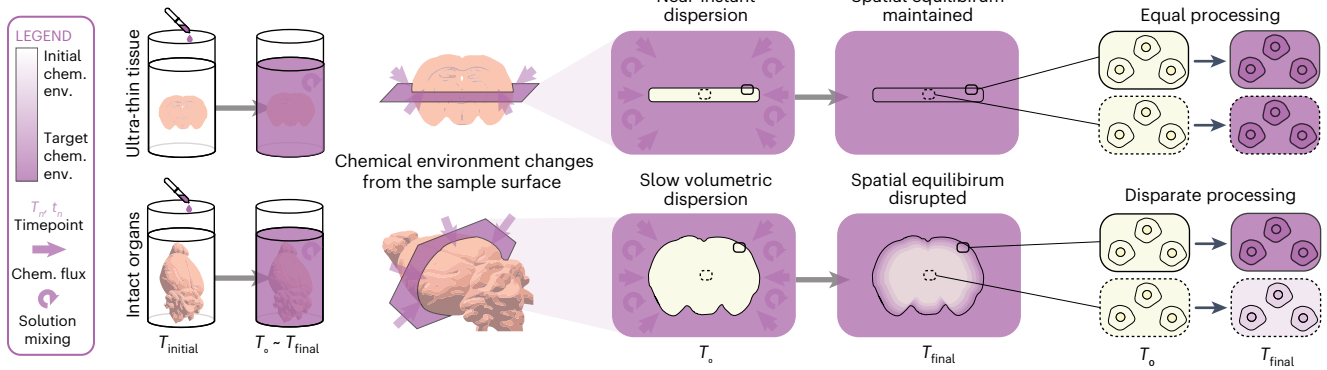
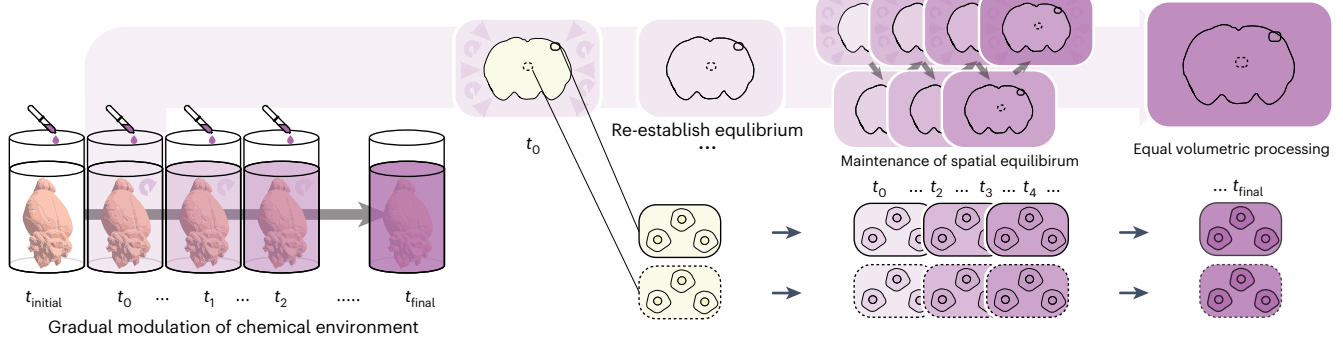
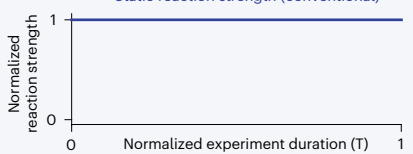
Results

Computational modeling of CuRVE

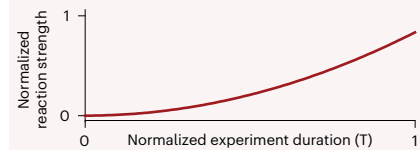
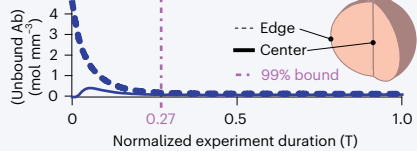
To achieve volumetric processing of cells for organ-wide quantitative single-cell analysis, the chemical environment (for example, antibody concentration) needs to be uniformly maintained throughout the tissue volume. For instance, in conventional immunolabeling methods, antibodies immediately start reacting with antigens as they are being diffused throughout a tissue. Due to the rapid consumption of antibodies compared to their dispersion rate, different parts of the tissue experience drastically different chemical environments. This issue is exacerbated in thicker tissues and results in uneven labeling and incomplete antibody penetration^{20,25,34}.

In immunolabeling, we hypothesized that, by gradually shifting antibody–antigen binding equilibrium from a minimal binding state to a normal binding state, unevenly distributed antibodies resulting from slow diffusion and local antibody consumption could be redistributed, thereby restoring a volume-wide equilibrium before subsequent minute changes in antibody–antigen binding equilibrium occur. If this gradual adjustment of the binding equilibrium occurs at a rate that allows for the maintenance of a spatially uniform distribution of antibodies at any given moment, all cells within the intact tissue could experience the same antibody labeling conditions, thus achieving complete and uniform immunolabeling of all cells in large-scale intact tissues (Fig. 1b).

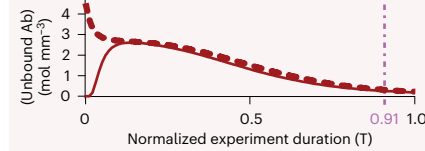
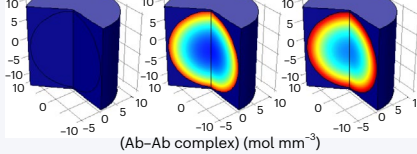
To present a proof-of-concept demonstration, we developed a computational simulation that models (1) the diffusion and conservation of antibodies; (2) dynamic equilibrium of antibodies (Ab), antigens (Ag) and their complexes (Ab–Ag); and (3) the concentration-dependent second-order kinetics of Ab–Ag reaction (Supplementary Note 1). We modeled the application of CuRVE under two scenarios: with simple diffusion and with stochastic electrotransport (SE). SE increases the transport rate of molecules by several orders of magnitude to enable rapid tissue processing³⁵, which substantially lowers the barrier for shifting the reaction–transport balance. This computational model allows for a comparative analysis between conventional static reaction strength approaches and systems implementing CuRVE. The gradual shifting of binding equilibrium required to achieve CuRVE is approximated by the sweeping of antibody reaction rate, contrasting a standard constant reaction (Fig. 1c and Extended Data Fig. 1a).

a Passive dispersion of chemical environment**b** Continuous redispersion of volumetric equilibrium (CuVE)**c** Static reaction strength (conventional)

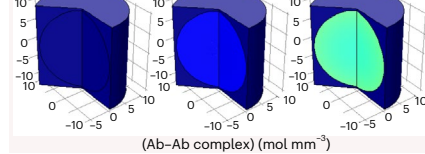
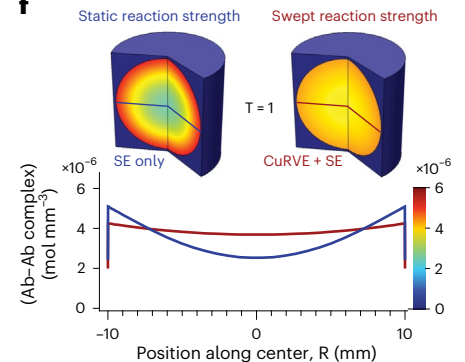
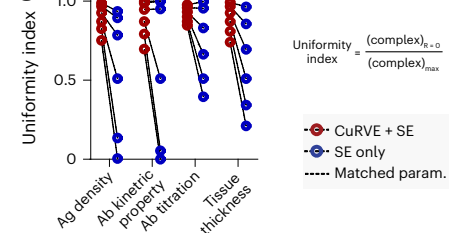
Swept reaction strength (CuVE)

**d** SE only

CuVE + SE

**e** SE only

CuVE + SE

**f****g****Fig. 1 | Conceptual description and computational modeling of CuVE.**

a, Schematic description comparing conventional chemical processing of ultra-thin tissues and intact tissues. Ultra-thin tissues experience near-instant dispersion of chemical environment, allowing equal processing of all cells. Intact organs experience slow volumetric dispersion, leading to disruption of spatial equilibrium and, thus, disparate cellular processing. **b**, Schematic description of CuVE for equal volumetric processing. Chemical environments are shifted gradually and allowed to re-establish equilibrium before proceeding with the subsequent gradual shift. With the continuous maintenance of spatial equilibrium, all cells can experience equal processing through the volume. **c–g**, Computational modeling of CuVE in COMSOL for volumetric immunolabeling. Model for conventional constant reaction methodology, static binding strength (left, blue line). Model for CuVE, swept binding strength (right, red line). **c**, Normalized reaction strength modulation through time. **d**, Concentration of unbound antibodies evaluated near the surface (dotted

line) and the center (solid line) throughout the simulation duration. Purple vertical dotted lines indicate the timepoint where 99% of the antibody–antigen complexes are formed relative to $T = 1$. Static, SE only (left); Swept, CuVE + SE (right). **e**, Concentration of antibody–antigen complexes throughout the volume represented by a color heatmap. Timepoints shown are relative to the 99% bound timepoint indicated in **d**. $T = 0, 0.09$ and 0.18 for SE only. $T = 0, 0.3$ and 0.6 for CuVE + SE. **f**, Overlaid concentration profiles of antibody–antigen complexes through the center of the volume at the end of the simulation. Volume rendering of the SE-only model (left) and the CuVE + SE model (right). **g**, Sensitivity analysis via parametric sweep of antigen density, forward reaction rate, antibody-to-antigen ratio and tissue thickness. The uniformity index represents the flatness of the concentration profile given by concentration at center divided by maximum concentration at $T = 1$. Data points evaluated with matching parameters are linked via dotted lines.

When simulating a conventional constant reaction scenario, evaluation of the unbound antibody concentration revealed that the core and the surface regions of the tissue experience vastly different antibody concentrations throughout the simulation (Fig. 1d, Extended Data Fig. 1b and Supplementary Video 1). Conversely, the use of swept reaction rate allowed the concentrations of unbound antibodies in the core and the surface to converge throughout the experiment (Fig. 1d, Extended Data Fig. 1b and Supplementary Video 1). This results in gradual and uniform formation of Ag–Ab immune complexes throughout the whole volume and throughout the experiment, as opposed to the classical propagation of the reaction front observed with the conventional approach (Fig. 1e, Extended Data Fig. 1c and Supplementary Video 1). The final concentration profiles of the immune complexes through the centerline of the volume indicates near uniform profile for the CuRVE approach compared to graded profile of the constant reaction approach, both evaluated with identical parameters (Fig. 1f, Extended Data Fig. 1d and Supplementary Video 1). Although both scenarios with simple diffusion and SE showed considerable improvement of labeling uniformity, SE enabled realization of the CuRVE approach without the need for extended experimental duration. This underscores the importance of enhanced SE transport and its synergy with CuRVE.

Moreover, the CuRVE approach exhibited substantially reduced sensitivity against changes in various experimental parameters (for example, antigen density and amount of antibody used). In general, organ-scale immunolabeling represents a complex optimization problem due to heterogeneity of tissue properties, target abundance and probe properties^{36,37}. We compared the sensitivity of both reaction modes against these variabilities through systematic simulations across wide ranges of parameters. The CuRVE configuration robustly maintained uniform labeling across the volume compared to the constant reaction mode (Fig. 1g). Furthermore, comparing the CuRVE approach to simulations of SWITCH or partial inhibition of reaction strength (Extended Data Fig. 1e,f) revealed its potential to be especially robust against variabilities in antigen density and antibody kinetic properties (Extended Data Fig. 1g). The low sensitivity of CuRVE to experimental variables has the potential to greatly reduce the time and cost associated with the laborious optimization. Taken together, our computational model demonstrates that the implementation of CuRVE enables equal processing of all individual cells in organ-scale tissue to achieve uniform volumetric labeling across a broad range of commonly confronted experimental parameters, preventing technical biases that may affect biological interpretations.

Implementing of CuRVE for ultra-fast volumetric immunolabeling

To implement CuRVE for volumetric immunolabeling, we used SE³⁵ for expedited transport of chemicals. While allowing equal volumetric processing, implementing CuRVE will extend the time needed for the overall experiment. The computational modeling depicts a scenario where the swept reaction mode could take approximately three times longer to complete (Fig. 1d). Therefore, any implementation of CuRVE will benefit substantially from adopting increased transport of chemicals. Penetration of antibodies in mouse brains can take from days to weeks depending on the probe, target and the methodology^{21,38}. SE significantly accelerates dispersion of chemicals and molecular probes while preventing damage to biological tissues³⁵.

Next, we assessed various strategies for modulating antibody binding kinetics. Antibodies, as biological immune components, are often the most reactive in physiological conditions, and changes to pH, temperature and ionic strength can significantly impact their binding kinetics³⁹. However, due to the natural heterogeneity of antibodies, varying one factor alone is not enough to broadly regulate their kinetics. Thus, we hypothesized that combining two different modulation factors could improve the overall compatibility of the methodology. Antibody

interactions can be disrupted by the presence of detergents, and we screened various chemicals for their effect on standard immunohistochemistry. Dodecylsulfuric acid is an effective antibody binding inhibitor used previously for discrete control of antibody binding; however, it is less suitable for gradual modulation as it strongly inhibits protein interaction even at extremely low concentrations^{19,40}. Instead, deoxycholic acid, a unique bile acid with high pKa and greater polydispersity in micelle size^{41,42}, can modulate binding affinity of various antibodies in a concentration-dependent and pH-dependent manner⁴⁰ (Fig. 2a,b and Extended Data Fig. 2a). Deoxycholic acid also increases the rate of antibody transport by increasing the net charge and electromobility of antibodies through cooperative complex formation⁴³ (Extended Data Fig. 2b,c), which can further improve molecular transport. Together, these properties of deoxycholic acid render it an ideal master regulator for effectively modulating binding conditions of various antibodies for enabling CuRVE for volumetric immunolabeling.

Next, to achieve a gradual pH sweep in an automated and reproducible manner, we took advantage of electrochemical reactions that naturally occur during SE. Leveraging the electrocatalytic oxidation of D-sorbitol that produces acidic byproducts, such as formic acid⁴⁴, we achieved gradual sweep of pH from 9.55 to 8.1 over the course of 24 h in a highly reproducible and automated manner (Fig. 2c,d). To achieve a gradual modulation of the concentration of sodium deoxycholate (NaDC), the salt form of deoxycholic acid, we took advantage of the nanoporous membrane used to separate the large volume of conductive buffer and the small volume of molecular-probe-enriched labeling buffer. By carefully choosing the porosity of regenerated cellulose membrane, we achieved reproducible sweeping of NaDC concentration mediated by the diffusion of deoxycholate monomers throughout the 24-h period (Fig. 2c), where the initial concentration of 1.05% (w/v) NaDC reduces to 0.13% (w/v) NaDC (Fig. 2d and Extended Data Fig. 2e). Furthermore, to ensure that electrocatalytic oxidation of the buffer did not affect antibody binding, we processed the eFLASH buffer and tested its initial and terminal state with 24 different antibodies, confirming strong binding in the terminal state (Extended Data Fig. 2d). We named this system eFLASH as an expedited practical implementation of the CuRVE framework for volumetric immunolabeling.

Finally, to demonstrate the effectiveness of eFLASH, we stained both hemispheres from the same adult mouse brain with and without binding affinity modulation using the same amount of antibodies within 1 d (Fig. 2e,f and Supplementary Video 2). Each hemisphere was stained with 5 μ g of anti-neurofilament (NF) antibody, a pan-axonal marker, and 3 μ g of anti-calbindin (CB) antibody, an interneuron marker. SE-labeled hemisphere shows heavily graded labeling from the surface to the center (Fig. 2e–i–iii and Supplementary Video 2), indicating antibody depletion and the necessity for substantially larger antibody quantities to improve probe penetration using the constant reaction approach. In contrast, eFLASH-labeled hemisphere shows uniform labeling of CB⁺ interneurons and NF⁺ axons throughout the sample even with such a small amount of antibody. This outcome is attributed to the CuRVE process effectively preventing probe depletion and ensuring equal processing of all cells within the intact sample (Fig. 2f and Supplementary Video 2). This result demonstrates the power of adopting CuRVE in combination with SE to achieve uniform, cost-effective and ultra-fast labeling of large-scale tissues.

Universal applicability of eFLASH

Using eFLASH, we achieved rapid and uniform labeling of whole mouse organs, whole rat brain, marmoset brain block as well as human cerebral organoids and human brain block while also demonstrating simultaneous labeling of three different antibodies with the same 1-d immunolabeling protocol. The whole rat brain with dimensions 15.3 mm (lateral axis), 23.3 mm (A-P axis) and 11 mm (D-V axis) was uniformly labeled with anti-neuronal nuclei (NeuN) (Fig. 3a and Supplementary Video 3) within just 1 d, including densely packed populations such as hippocampal

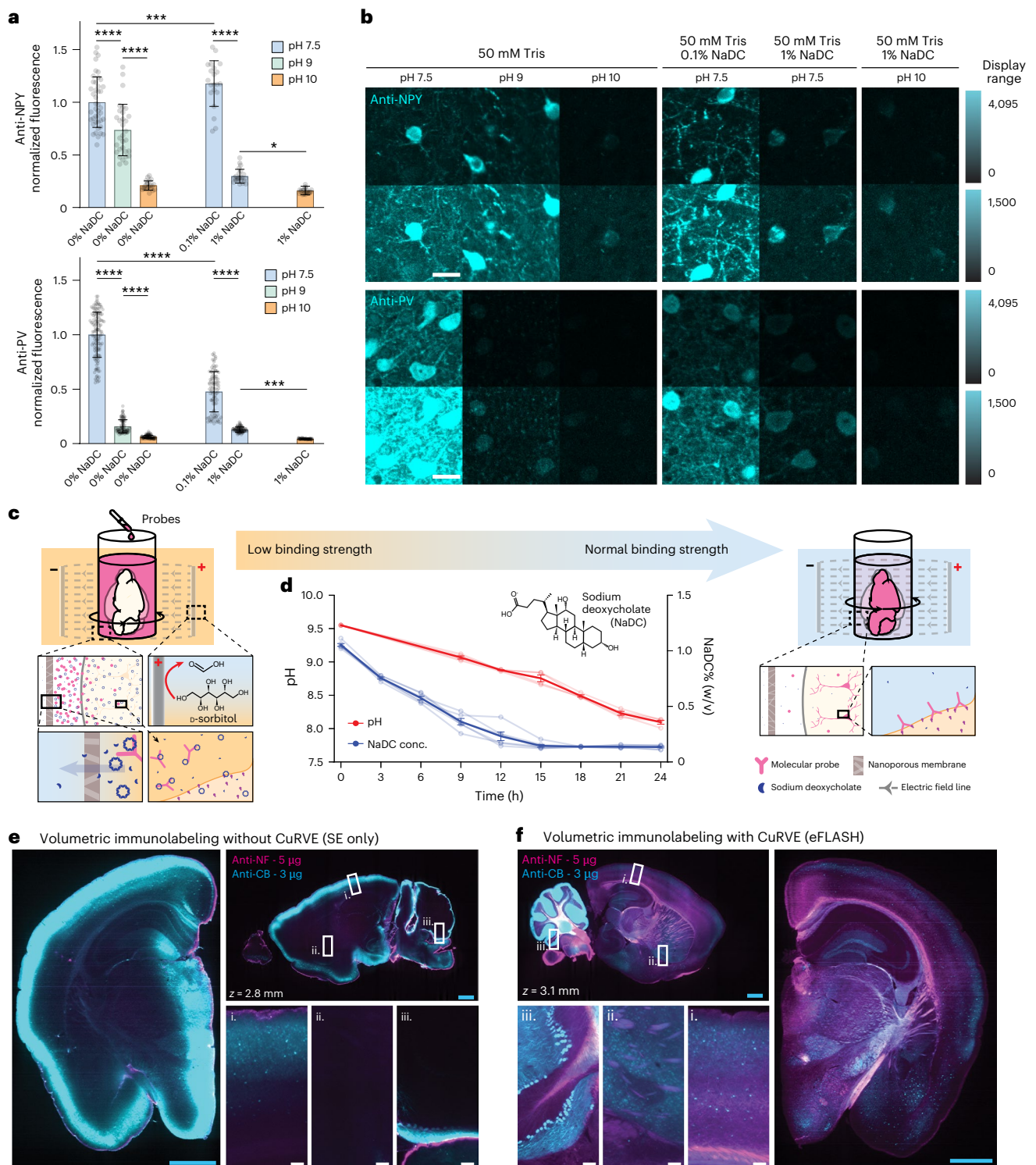


Fig. 2 | Design and validation of the eFLASH system. a, Effect of pH and NaDC concentration on binding of anti-NPY and anti-PV antibodies. Normalized average soma fluorescence intensities ($n = 3$ independent experiments for each buffer condition, each soma shown as an individual data point; total segmented soma: NPY = 160, PV = 256). One-way ANOVA multiple comparisons, mean \pm s.d. **** $P < 0.0001$; *** $P = 0.0003$ (anti-PV 1% NaDC, pH 7.5 versus pH 10); *** $P = 0.0004$ (anti-NPY pH 7.5, 0% NaDC versus 0.1% NaDC); * $P = 0.0243$ (anti-NPY 1% NaDC, pH 7.5 versus pH 10). **b**, Representative images for data in **a** shown in two different display ranges: 0/4,095 (top row) and 0/1,500 (bottom row). Scale bar, 20 μm (white). **c**, Schematic of the eFLASH system. The pH and NaDC concentration of the labeling solution are gradually reduced to sweep the molecular probes' binding affinity from low to normal binding strength in the context of SE. Electrocatalytic oxidation of D-sorbitol on the anode surface

generates acidic components that lower pH. NaDC concentration of the labeling solution is reduced by the diffusion of NaDC monomers through the nanoporous membrane. **d**, Measurement of pH ($n = 4$ independent experiments) and NaDC concentration ($n = 6$ independent experiments) throughout the 24-h processing. Mean \pm s.e.m. **e, f**, Volumetric labeling of two hemispheres of a single brain with SE and eFLASH, respectively, using the same mass of antibodies: 3 μg of anti-CB (calbindin) and 5 μg of anti-NF (neurofilament marker). Optical plane of 3D volumetric data. 20- μm MIPs. Sagittal (original imaging plane) and coronal (reconstructed plane). Distance of the sagittal optical plane from the medial plane: $z = 2.8$ mm (**e**) and $z = 3.1$ mm (**f**). Zoomed-in view of the coronal layers (**e-i** and **f-i**), striatum (**e-ii** and **f-ii**) and cerebellum (**e-iii** and **f-iii**). Scale bars, 2 mm (cyan) and 100 μm (white). $n = 2$ independent experiments. MIP, maximum intensity projection.

dentate granule cells (Fig. 3a-ii) and cerebellar granule cells (Fig. 3a-iv). eFLASH can uniformly label extremely densely expressed proteins, such as PV (Fig. 3b and Supplementary Video 4), in challenging regions, such as reticular nucleus of the thalamus (Fig. 3b-iii) and cerebellum. As a demonstration of triple volumetric immunolabeling, we performed one-shot labeling of anti-NeuN, anti-tyrosine hydroxylase (TH) and anti-choline acetyltransferase (ChAT), capturing all neurons and projections to dissect the dopamine-based (TH) and acetylcholine-based (ChAT) diffuse modulatory systems (Fig. 3c and Supplementary Video 5), with high-quality labeling that can clearly delineate populations, such as the cholinergic neurons in laterodorsal tegmental nucleus and dopaminergic neurons in locus coeruleus (Fig. 3c-iii).

eFLASH is also compatible with multiple rounds of labeling, making it particularly advantageous for precious samples, as those derived from non-human primates and humans. We performed two separate rounds of uniform labeling on marmoset visual cortex with anti-PV (Fig. 3d) and anti-neuropeptide Y (NPY) (Fig. 3e and Supplementary Video 6), identifying disparate distributions for both PV⁺ and NPY⁺ neurons compared to those in mouse visual cortex. In marmoset, we observed variable distribution of PV⁺ cells across the visual cortical layers, contrasting with the more uniform distribution seen in mouse visual cortex (Fig. 3d-i,ii). Furthermore, NPY⁺ cells in the marmoset visual cortex were mostly localized to deep regions beyond layer IV and into white matter, whereas, in the mouse cortex, anti-NPY cells were more evenly distributed across the cortical layers (Fig. 3e-i,ii).

Additionally, to demonstrate the utility of eFLASH beyond neuroscience, using one single protocol without any additional optimization besides antibody validation, we performed immunolabeling of mouse embryo (Fig. 3f), mouse intestine, mouse liver lobule, mouse lung, mouse ear canal and mouse heart as well as human cerebral organoid and human brain block (Extended Data Fig. 3). Altogether, we demonstrated uniform volumetric immunolabeling of various cell-type-specifying markers (for example, PV, CB, CR, NPY, SST, TH, TPH2, ChAT, VIP, nNOS, NeuN, GFAP, Iba1, TBR1 (ref. 45), SOX2 (ref. 45) and vimentin), structural markers (for example, α -SMA, β -tubulin, SMI-312 (pan-axonal), Neurofilament-L, Neurofilament-M and Neurofilament-H), neuronal activity proxy (for example, cFos⁴⁶) and other non-antibody molecular probes (for example, SYTO 16 and lectin) (Fig. 3a-f, Extended Data Fig. 4 and Supplementary Table 1). Together, these results demonstrate that eFLASH is a universal platform compatible with a wide range of tissue types and molecular probes without the need for laborious optimization procedures.

To demonstrate the versatility of eFLASH, we labeled intact tissues from mice, rats, marmosets and human organoids with 62 antibodies and two molecular probes. The affinity sweeping mechanism of eFLASH renders the technique robust against variabilities in tissue and antibody properties, enabling the use of the same operational parameters for a wide range of samples. With electrophoretically enhanced molecular dispersion, eFLASH can label rodent organ-scale tissues, including whole rat brains, within just 1 d. Together, these results demonstrate that eFLASH is a universal platform compatible with a wide range of tissue types and molecular probes without the need for laborious optimization procedures.

Comparison of genetic and protein-based cell type labeling

To demonstrate the power of quantitative organ-scale immunohistological cell profiling, we used eFLASH to compare genetic and protein-based cell type labeling in two widely used transgenic labeling methods: Cre-*LoxP* and bacterial artificial chromosome (BAC) transgene⁴⁷⁻⁵⁰. Cell type marker proteins are indispensable resources for cellular phenotyping as their expression can indicate specific cell lineages or characteristic physiological functions. Transgenic lines incorporating fluorescence reporters driven by the transcription of cell type marker genes have been extensively used to investigate organ-wide distribution of distinct cell types and their disease-specific changes^{49,51,52}.

However, several studies reported discrepancies between transcription activity and protein expression^{53,54}, known to occur due to varying degrees of leaky expression, poor inducibility and toxicity^{49,55-57}. Differences in protein expression levels and dynamics can contribute to such variations as well⁵⁸, underscoring the importance of organ-wide immunohistochemical protein expression analysis as a suitable approach to supplement or corroborate transgenic labeling.

First, we compared genetic and antibody-based labeling of PV-expressing cells, the largest class of GABAergic inhibitory neurons, in intact mouse brains. To prevent the decay of the genetically expressed fluorescent proteins, we performed SHIELD preservation, known to robustly conserve fluorescent signals¹², and then employed eFLASH to immunolabel a PV-Cre⁵⁹/*loxP*-tdTomato⁶⁰ double transgenic mouse hemisphere using an extensively validated anti-PV antibody (Fig. 4a-c). We conducted a brain-wide quantitative analysis comparing PV-tdTomato, a reporter fluorescent protein driven by the expression of PV gene, and anti-PV⁺ (that is, PV immunoreactive) signals, which revealed substantial discrepancies between the two labeling approaches. For imaging processing and detection of PV-tdTomato and anti-PV cells, we used our image analysis pipeline⁶¹, demonstrated on multiple cell type markers (Extended Data Fig. 5). Interestingly, the degree of mismatches varied considerably across different brain regions (Fig. 4b,c and Supplementary Video 7). Notably, in contrast to a high degree of correspondence between PV-tdTomato and anti-PV labeling in primary motor and primary somatosensory cortices (with 88% and 85% of co-positivity, respectively), a substantial fraction of tdTomato-labeled cells exhibited non-detectable PV protein levels in certain cortical areas (for example, 56% and 75% in piriform and lateral entorhinal cortex, respectively) as well as subcortical regions (45% in caudate putamen (CPU) and 62% in nucleus accumbens (Nac)). Furthermore, our analysis also revealed the presence of anti-PV⁺ populations that were not covered by genetic labeling. For example, in CPU and Nac, 66% and 77% of anti-PV⁺ cells, respectively, did not express detectable levels of tdTomato (Fig. 4b,c).

Next, we compared genetic and protein-based labeling of ChAT-expressing cells. The cholinergic system is known to have complex ChAT and vesicular acetylcholine transporter regulation, which can complicate transgenic approaches to label the whole system. ChAT^{BAC}-eGFP mice⁶² have been widely used to label cholinergic neurons in both central and peripheral nervous systems. We observed substantial divergence of enhanced green fluorescent protein (EGFP) expression from the ChAT immunoreactivity pattern (Fig. 4d-h and Supplementary Video 8). For example, in primary motor cortex (M1) and primary somatosensory cortex (S1), only 9% and 14% of EGFP⁺ cells were also anti-ChAT⁺, respectively. In hippocampal CA1 and CA3, only 0.2% and 0.3% of EGFP⁺ cells exhibited detectable levels of ChAT immunoreactivity. Additionally, substantial populations of ChAT immunoreactive cells without EGFP expression were observed, particularly in primary auditory and visual cortices (93% and 89%, respectively) (Fig. 4f). These discrepancies were heterogeneous even within the same brain region. For instance, in the nucleus accumbens ventral part, most anti-ChAT⁺ cells were also EGFP⁺ (80%), whereas, in its dorsal counterpart, only 26% of anti-ChAT⁺ cells were co-localized with EGFP⁺ (Fig. 4e-iii). Furthermore, 3D visualization of the hemisphere revealed labeling mismatch in fiber bundles, where we observed a brain stem fiber bundle composed of anti-ChAT⁺ axons without EGFP signals (Fig. 4g,h).

The use of transgenes for protein expression profiling is a complex and nuanced topic that necessitates a comprehensive understanding of gene dynamics and expression levels. For example, despite its wide applicability, CRE-dependent genetic targeting has a possibility of false-positive (for example, transgene-independent CRE expression), true-negative (for example, CRE mosaicism⁵⁶) and individually variable (for example, parental inheritance pattern) labeling^{56,63,64}. The exact strategy used for transgenic labeling directly influences the population

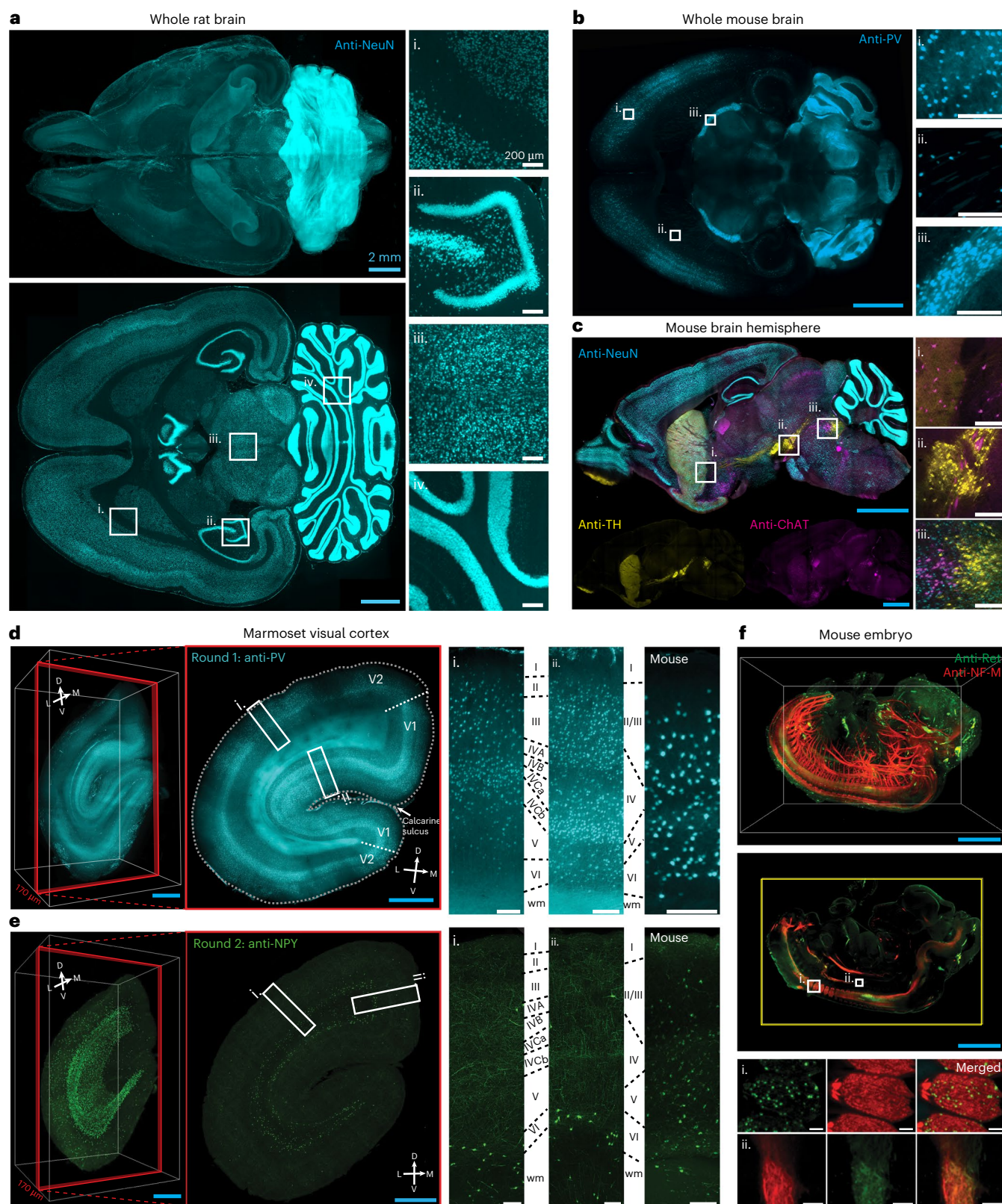


Fig. 3 | Rapid, uniform and universal volumetric immunolabeling using eFLASH. a, Whole volume rendering, representative optical section and magnified images (**a-i-iv**) of whole rat brain labeled with anti-NeuN (Supplementary Video 3). **b**, Representative optical section and magnified images (**b-i-iii**) of whole mouse brain labeled with anti-PV (Supplementary Video 4). **c**, Representative optical section and magnified images (**c-i-iii**) of mouse brain hemisphere simultaneously labeled with anti-NeuN, anti-TH and anti-ChAT antibodies (Supplementary Video 5). **d, e**, Whole volume rendering, representative

optical section (170- μ m MIP) and magnified images (**d-i,ii** and **e-i,ii**) of marmoset brain block containing visual cortex (5 mm \times 5 mm \times 8 mm) labeled with round 1: anti-PV (**d**) and round 2: anti-NPY (**e**) (Supplementary Video 6). **f**, Whole volume rendering, representative optical section and magnified images (**f-i,ii**) of mouse embryo labeled with anti-mouse Ret and anti-NF-M. Optical sections are 20- μ m MIP unless specified otherwise. Scale bars, 2 mm (cyan) and 200 μ m (white). MIP, maximum intensity projection; NF-M, Neurofilament-M; wm, white matter.

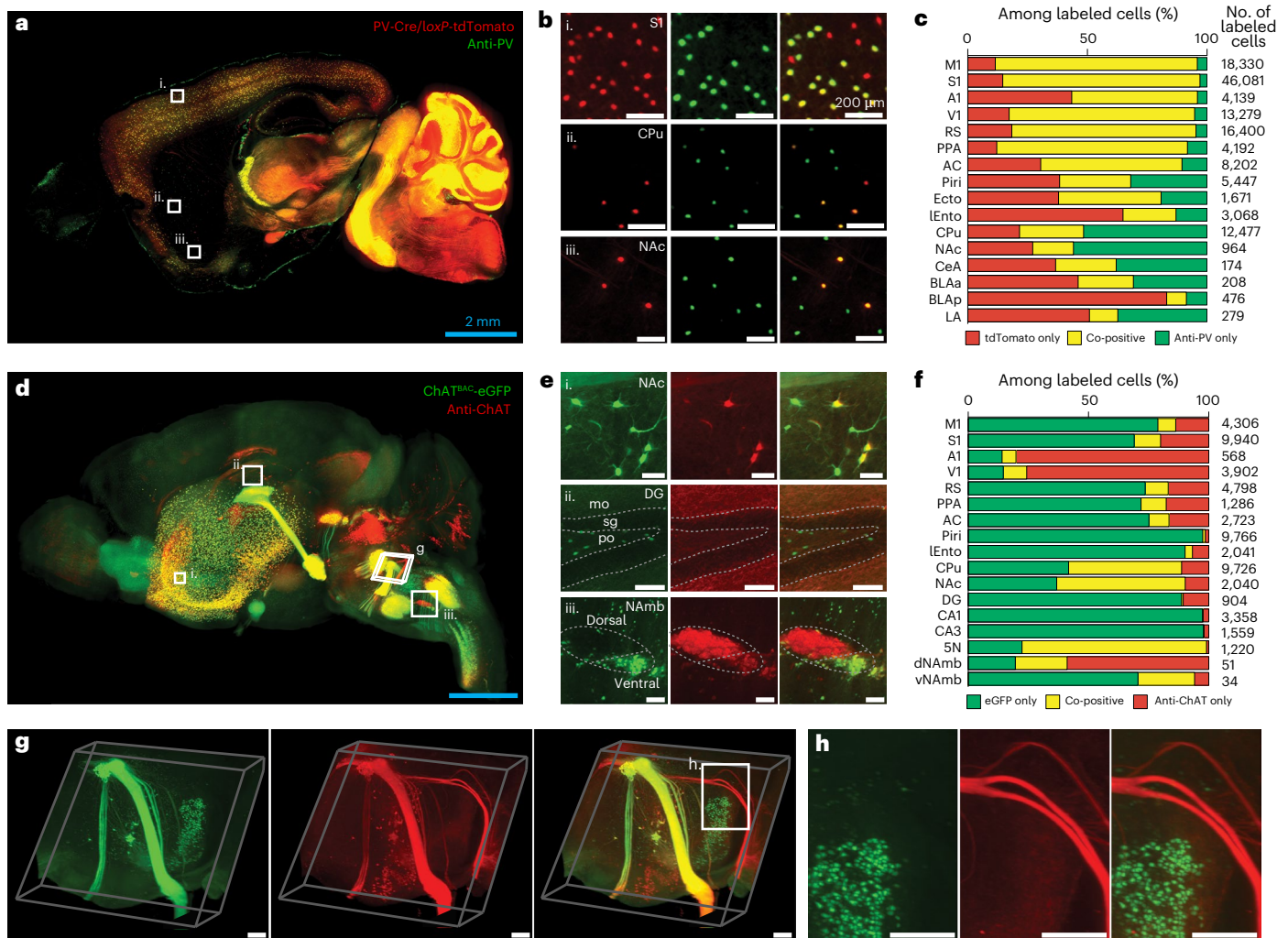


Fig. 4 | Holistic comparison of transgenic and immunolabeling-based cell type labeling. **a–c**, 3D dataset from a PV-Cre and *loxP*-tdTomato dual transgenic mouse hemisphere stained with anti-PV antibody. **a**, Representative optical section. **b**, Magnified images of **a**. **c**, A percentage plot for tdTomato-only (red), anti-PV-only (green) and tdTomato and anti-PV co-positive cells (yellow) among all the labeled cells in individual representative brain regions. **d–h**, 3D dataset of a ChAT^{BAC}-eGFP mouse brain stained with anti-ChAT antibody. **d**, Whole volume rendering. **e**, Magnified images of **d**. **f**, A percentage plot for EGFP-only (green), anti-ChAT-only (red) and EGFP and anti-ChAT co-positive cells (yellow) among all the labeled cells in individual representative brain regions. **g**, Magnified view of

d, h, Zoom-in view of **g**. Scale bars, 2 mm (cyan) and 200 μ m (white). 5N, motor nucleus of trigeminal; A1, primary auditory cortex; AC, anterior cingulate cortex; BLAa, basolateral amygdala, anterior part; BLAp, basolateral amygdala, posterior part; CA1, hippocampal CA1; CA3, hippocampal CA3; CeA, central amygdala; DG, dentate gyrus; dNAmb, nucleus ambiguus, dorsal part; Ecto, ectorhinal cortex; LA, lateral amygdala; IEnto, lateral entorhinal cortex; mo, dentate gyrus, molecular layer; po, dentate gyrus, polymorph layer; Piri, piriform cortex; PPA, posterior parietal association cortex; RSA, retrosplenial cortex; sg, dentate gyrus, granule cell layer; V1, primary visual cortex; vNAmb, nucleus ambiguus, ventral part.

of neurons labeled, and, with the most commonly used transcription activation-based binary systems (for example, Cre/*loxP* binary system), all cells expressing the target protein at any point during their development will be labeled with the reporter proteins⁶⁵. Hence, although the discrepancies between transient target protein expression and cumulative reporter protein expression were previously described in part, the degree of discrepancies observed brain wide here highlights the necessity for holistic validation. These results suggest that eFLASH can enable holistic and unbiased organ-wide single-cell immuno-profiling, offering a precise and specific snapshot of endogenous protein levels, which can effectively complement and validate the transgenic labeling approach.

Variable PV immunoreactivity in healthy wild-type mice

While investigating the discrepancy between transgenic labeling and immunolabeling of PV neurons in PV-Cre⁵⁹/*loxP*-tdTomato⁶⁰ mice, we observed significant regionalized loss of anti-PV⁺ neurons in both wild-type and reporter mice. PV is a calcium-binding protein, and

neurons expressing PV are known to play a key role in regulating brain functions, with their disruptions associated with neuropsychiatric conditions, including schizophrenia, bipolar disorder and autism spectrum disorder (ASD)⁶⁶. Notably, both individuals with ASD and ASD mouse models were reported to show reduced numbers of PV⁺ cells^{66,67}, and schizophrenia mouse models exhibited decreased PV immunoreactivity in the prefrontal cortex⁶⁸. Previously, the large regionalized loss of anti-PV⁺ neurons was observed and described as ‘parvalbumin holes’ for mice with deficits in GFR α 1 signaling⁶⁹; however, to our knowledge, we are the first to report the observation of this phenomenon in healthy wild-type mice with holistic whole brain data. We observed this phenotype of regionalized reduction of PV, henceforth named low-PV zone (LPZ), in both eFLASH-labeled whole brains as well as in conventionally labeled tissue sections from healthy wild-type adult mice (Extended Data Fig. 6 and Supplementary Video 9). For this validation, we sourced animals from three separate institutes to further control the impact of environmental variability on this phenotype.

Interestingly, high-resolution confocal imaging revealed that the large regions with unusually low density of anti-PV⁺ somas still maintained a robust network of anti-PV⁺ processes as well as inhibitory synapses marked by anti-Gephyrin immunolabeling (Fig. 5a–i). However, we did observe reduction of inhibitory PV⁺/Gephyrin⁺ synapses (Extended Data Fig. 7a–c), potentially suggesting reduction of inhibitory activity in the low PV density regions. We conducted an additional round of immunolabeling of eFLASH-labeled sample using traditional passive immunohistochemistry with a different PV antibody (Fig. 5b). Signals from two different PV antibodies fully overlapped, verifying the observed discrepancy between anti-PV⁺ and PV-tdTomato signal in Fig. 4a,b. We also observed that PV-tdTomato signal persisted in LPZ (Extended Data Fig. 7d,e). Additionally, LPZ was not associated with loss of neuron or nuclei density, and LPZ borders were not correlated with the distribution of CB immunoreactive cells, another calcium-binding interneuron marker (Fig. 5c, Extended Data Fig. 7f–h and Supplementary Video 9).

To holistically characterize LPZs and compare the population of PV-tdTomato⁺ and anti-PV⁺ neurons, we conducted brain-wide phenotyping of seven age-matched postnatal day (P) 56 male PV-Cre/*loxP*-tdTomato double transgenic mice, three of which were littermates (denoted as brains 1–3). We observed that LPZs with extremely sparse anti-PV⁺ somas still had robust PV-tdTomato labeling (Fig. 5d and Supplementary Video 10), and these regions with mismatch in PV-tdTomato and anti-PV labeling were observed in all mice. We observed high individual variability in total LPZ volumes (Fig. 5f) of LPZs and their locations (Fig. 5e,g), even among littermates, often with significant lateral differences across hemispheres. Genetically labeled PV cells (tdTomato⁺) exhibited consistent densities across all mouse brains, and we did not observe associated changes to tdTomato⁺ somas in LPZs (Fig. 5d,h). Immunolabeled PV⁺ cells (anti-PV⁺) showed significantly reduced density with high individual variabilities in areas such as prefrontal, infralimbic, frontal pole and the orbital regions of the cerebral cortex (Fig. 5g,i).

As the PV-Cre/*loxP*-tdTomato reporter line both captures cumulative expression of PV and amplifies neurons with low expression of PV, the observed discrepancy potentially suggests a large-scale downregulation of PV expression during mice development. Because of the high individual and lateral variability of the observed phenotype, identification through slice-based immunohistochemistry may be challenging. To interrogate disease-specific cellular and molecular changes as well as to evaluate and validate genetic tools, it is crucial to establish accurate baselines for any given animal model. Population averages can be useful for establishing such a baseline, but they cannot capture the degree of individual variabilities. This finding demonstrates the importance and the utility of scalable volumetric immunolabeling tools such as eFLASH to provide unbiased holistic high-resolution organ-wide characterizations.

Discussion

Here we introduced CuRVE in nanoporous matrices as a conceptual framework for uniform volumetric processing. In the case of biological tissues, the uniform processing would reduce bias and ensure faithful single-cell-level analyses akin to those done on dissociated cells. Because of the inherently high density of biological tissues, even with extensive permeabilization, chemical processing of intact tissue often suffers from slow diffusive mass transfer. The CuRVE approach offers a solution to navigating this transport-limited regime by slowing down the reactions so that the dispersion of reactants can re-establish volumetric equilibrium at any given moment before a subsequent minute change in reaction strength occurs. Both reversible and irreversible reactions will be compatible with CuRVE as long as the ratio between the reaction rate and the transport rate, essentially the Damköhler number, can be manipulated to remain low enough for a given system to achieve sufficiently uniform processing.

In the context of volumetric immunolabeling, reaction–diffusion modulation has been extensively investigated to achieve organ-scale labeling (for example, SWITCH¹⁹, CUBIC-HV¹⁷ and Thick/SPEARs²¹), and other innovative methods to reduce the diffusion length achieved whole rodent body (vDISCO²⁰/wildDISCO³⁰) and human brain slab (ELAST²²/mELAST⁷⁰) immunolabeling. However, further advancements in practicality, versatility and data quality are necessary to accelerate more widespread adaptation and use of volumetric immunolabeling by the wider research community. The CuRVE framework offers an approach for addressing some of these challenges by enhancing the efficiency and flexibility of labeling techniques. Here we demonstrated eFLASH as a proof-of-concept implementation of CuRVE for an ultra-fast, versatile and scalable immunolabeling of organ-scale tissues. The increased throughput, scalability, low reagent requirement of eFLASH is not mutually exclusive to other technologies if the tissue can withstand electrophoresis, offering options for orthogonal optimizations and improving equal processing of all cells.

Our discovery of large regionalized loss of PV-immunoreactive neurons in healthy adult mice with high individual variability emphasizes the importance of holistic and unbiased phenotyping. In mouse adolescence, PV expression in prefrontal cortex is known to substantially increase and last to adulthood^{71,72}, and loss of PV expression in prefrontal cortex is associated with neurodegenerative models^{66–68}. As we observed robust presence of PV immunoreactive processes in LPZs (Fig. 5a), it is still possible that overall activity of PV-expressing synapses may remain high; however, the absence of PV-expressing neuronal bodies at such a large scale in healthy wild-type animals challenges existing preconceptions about transience of neuronal cell types and developmental neurobiology.

Future applications of eFLASH reside on multiple fronts. Multiplexed proteomic investigation remains a major challenge, especially in organ-scale tissues. Toward that end, the use of oligo-nucleotide conjugated antibodies offers great promise by taking advantage of the combinatorial barcoding capabilities as well as rapid and reliable probe exchange^{73,74}. The superior throughput and probe-insensitive nature of eFLASH will be an important asset for one-shot delivery and labeling with a large library of oligo-conjugated antibodies for realizing highly multiplexed spatial proteomics. The capacity of eFLASH to enable rapid delivery of bulkier alternative dyes, such as tandem fluorescent dyes, quantum dots and Raman-dyes³⁴, also holds possibilities for higher multiplexed molecular profiling of organ-scale tissues beyond the limited multi-color imaging barrier of conventional fluorescent dyes. Furthermore, there is a lot of room for optimization to speed up the process even further, which may be necessary for highly multiplexed organ-scale proteomics.

Here we demonstrated eFLASH with SHIELD-processed tissues for its robust preservation of endogenous fluorescent protein signals. One immediate limitation is that the use of eFLASH with other types of tissue preparation may first require additional optimizations and validations. eFLASH also shares the limitation of all immunolabeling applications that rely on the accuracy, quality and availability of commercial antibodies. Application of eFLASH on extremely large samples, such as macaque or human brain-sized tissue, may require additional innovations to ensure adequate dissipation of heat caused by joule heating under electrophoresis. Finally, eFLASH requires the use of specialized SE equipment to manage electrophoresis and cooling; however, commercial instruments are already available with batch processing capabilities.

The newly introduced tissue processing platform of CuRVE approaches the challenge of volumetric processing with a new perspective that focuses on enabling equal processing of all cells throughout the volume for organ-scale quantitative single-cell analysis while maintaining their spatial contexts. With eFLASH, we demonstrated that rapid and uniform immunolabeling is possible for organs as large as a whole rat brain within only 1 d. With the discovery of the LPZs, we

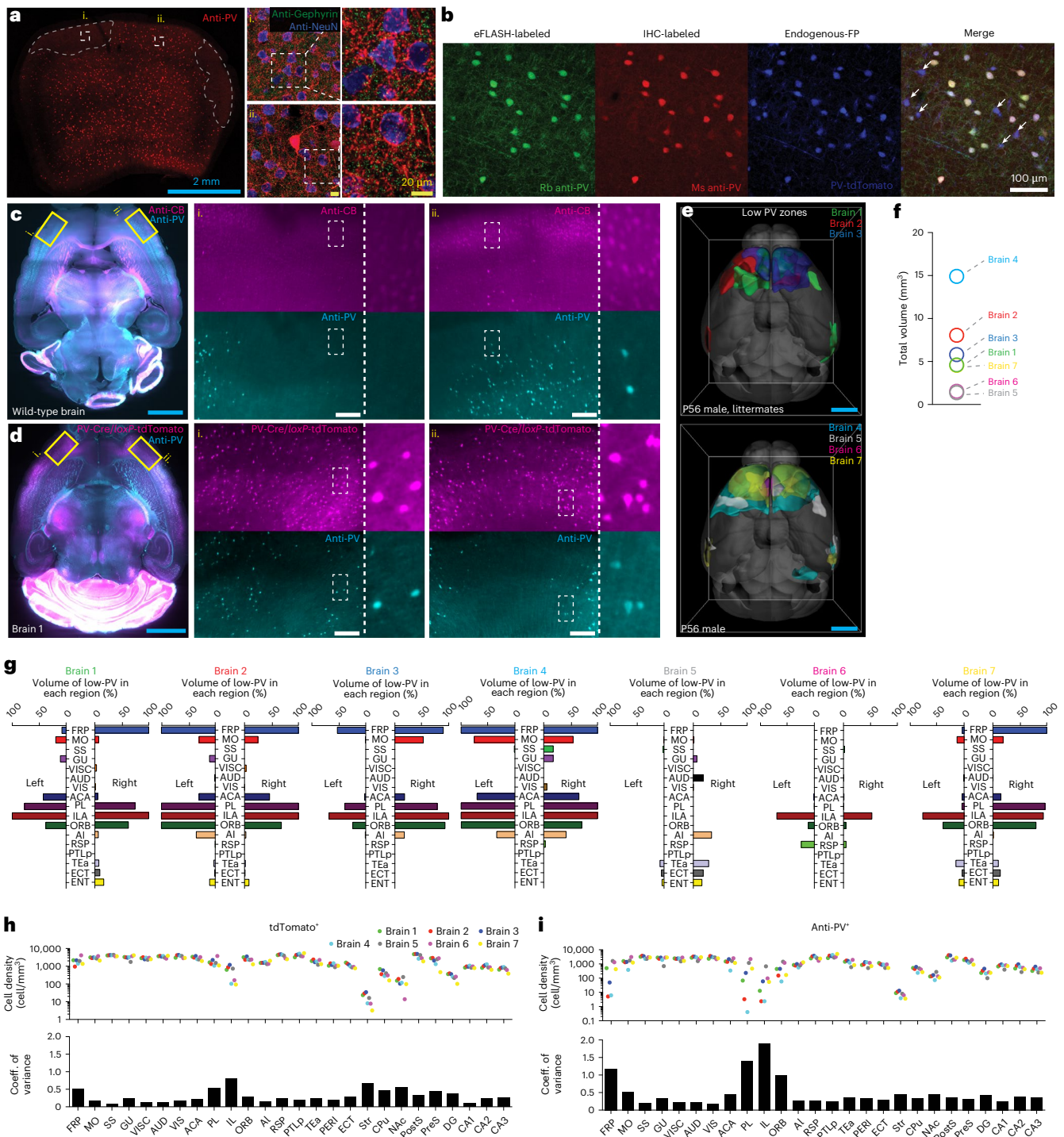


Fig. 5 | Significant individual variability of anti-PV⁺ expression in wild-type and PV-Cre/loxP-tdTomato mice. a, High-resolution imaging of LPZ (a-i) and normal region (a-ii), labeled with anti-PV, anti-Gephyrin and anti-NeuN in wild-type mouse ($n = 5$ animals). **b**, Additional round of immunolabeling of eFLASH-labeled tissue (with rabbit host anti-PV, green) using mouse host PV antibody (red). White arrows indicate PV-Cre/loxP-tdTomato expression (blue) that is disparate from both antibody labeling ($n = 3$ animals). **c**, Representative optical section of wild-type mice labeled with anti-PV (cyan) and anti-CB (magenta) and representative regions with LPZ (c-i,ii) with zoomed-in images ($n = 2$ animals). **d-h**, Seven PV-Cre and loxP-tdTomato double transgenic mouse brains were eFLASH labeled with anti-PV antibody. **d**, Representative optical section of PV-Cre/loxP-tdTomato (magenta) mice labeled with anti-PV (cyan) and representative regions with LPZ (d-i,ii) with zoomed-in images. **e**, 3D segmentation of low PV soma density regions in the seven brains. Brains 1–3 are littermates. **f**, Total volumes of low PV regions in individual brains. **g**, Quantification of the low PV region volumes in

each brain area in the left and right hemispheres. Brain-wide quantification of PV⁺ cells identified based on protein expression (h) and genetic fluorescent protein expression (i). Bottom row bar graph represents coefficient of variance for the regional densities among the seven brains. Scale bars, 2 mm (cyan), 100 μm (white) and 20 μm (yellow). 20- μm MIP optical sections. ACA, anterior cingulate area; AI, agranular insular area; AUD, auditory areas; CA1, hippocampal CA1; CA2, hippocampal CA2; CA3, hippocampal CA3; DG, dentate gyrus; ECT, ectorhinal area; ENT, entorhinal area; FP, fluorescent protein; FRP, frontal pole of the cerebral cortex; GU, gustatory areas; IHC, immunohistochemistry; IL, infralimbic area; MIP, maximum intensity projection; MO, somatomotor areas; ORB, orbital area; PL, prelimbic area; PostS, postsubiculum; PreS, presubiculum; PTLp, posterior parietal association area; RSP, retrosplenial area; SS, somatosensory areas; Str, striatum; TEa, temporal association areas; VIS, visual areas; VISC, visceral area.

demonstrated the necessity of holistic and unbiased phenotyping that is cost-effective and scalable to a large number of samples to challenge pre-existing assumptions. We envision that the efficiency and scalability of eFLASH will be pivotal in establishing high-quality resources on baseline proteomic expression for evaluation of transgenic and pathological mammalian models as well as human clinical samples.

Online content

Any methods, additional references, Nature Portfolio reporting summaries, source data, extended data, supplementary information, acknowledgements, peer review information; details of author contributions and competing interests; and statements of data and code availability are available at <https://doi.org/10.1038/s41587-024-02533-4>.

References

1. Stuart, T. & Satija, R. Integrative single-cell analysis. *Nat. Rev. Genet.* **20**, 257–272 (2019).
2. McKinnon, K. M. Flow cytometry: an overview. *Curr. Protoc. Immunol.* **120**, 5.1.1–5.1.11 (2018).
3. Longo, S. K., Guo, M. G., Ji, A. L. & Khavari, P. A. Integrating single-cell and spatial transcriptomics to elucidate intercellular tissue dynamics. *Nat. Rev. Genet.* **22**, 627–644 (2021).
4. McGinnis, L. M., Ibarra-Lopez, V., Rost, S. & Ziai, J. Clinical and research applications of multiplexed immunohistochemistry and in situ hybridization. *J. Pathol.* **254**, 405–417 (2021).
5. Byron, S. A., Van Keuren-Jensen, K. R., Engelthaler, D. M., Carpten, J. D. & Craig, D. W. Translating RNA sequencing into clinical diagnostics: opportunities and challenges. *Nat. Rev. Genet.* **17**, 257–271 (2016).
6. Liu, H. et al. DNA methylation atlas of the mouse brain at single-cell resolution. *Nature* **598**, 120–128 (2021).
7. Yao, Z. et al. A transcriptomic and epigenomic cell atlas of the mouse primary motor cortex. *Nature* **598**, 103–110 (2021).
8. Schwanhüsser, B. et al. Global quantification of mammalian gene expression control. *Nature* **473**, 337–342 (2011).
9. Prabakaran, S., Lippens, G., Steen, H. & Gunawardena, J. Post-translational modification: nature's escape from genetic imprisonment and the basis for dynamic information encoding. *Wiley Interdiscip. Rev. Syst. Biol. Med.* **4**, 565–583 (2012).
10. Moffitt, J. R., Lundberg, E. & Heyn, H. The emerging landscape of spatial profiling technologies. *Nat. Rev. Genet.* **23**, 741–759 (2022).
11. Chung, K. et al. Structural and molecular interrogation of intact biological systems. *Nature* **497**, 332–337 (2013).
12. Park, Y.-G. G. et al. Protection of tissue physicochemical properties using polyfunctional crosslinkers. *Nat. Biotechnol.* <https://doi.org/10.1038/nbt.42813> (2018).
13. Susaki, E. A. et al. Whole-brain imaging with single-cell resolution using chemical cocktails and computational analysis. *Cell* **157**, 726–739 (2014).
14. Renier, N. et al. IDISCO: a simple, rapid method to immunolabel large tissue samples for volume imaging. *Cell* **159**, 896–910 (2014).
15. Arias, A., Manubens-Gil, L. & Dierssen, M. Fluorescent transgenic mouse models for whole-brain imaging in health and disease. *Front. Mol. Neurosci.* **15**, 958222 (2022).
16. Renier, N. et al. Mapping of brain activity by automated volume analysis of immediate early genes. *Cell* **165**, 1789–1802 (2016).
17. Susaki, E. A. et al. Versatile whole-organ/body staining and imaging based on electrolyte-gel properties of biological tissues. *Nat. Commun.* **11**, 1982 (2020).
18. Zhao, S. et al. Cellular and molecular probing of intact human organs. *Cell* **180**, 796–812 (2020).
19. Murray, E. et al. Simple, scalable proteomic imaging for high-dimensional profiling of intact systems. *Cell* **163**, 1500–1514 (2015).
20. Cai, R. et al. Panoptic imaging of transparent mice reveals whole-body neuronal projections and skull–meninges connections. *Nat. Neurosci.* **22**, 317–327 (2018).
21. Lai, H. M. et al. Antibody stabilization for thermally accelerated deep immunostaining. *Nat. Methods* **19**, 1137–1146 (2022).
22. Ku, T. et al. Elasticizing tissues for reversible shape transformation and accelerated molecular labeling. *Nat. Methods* **17**, 609–613 (2020).
23. Tainaka, K. et al. Whole-body imaging with single-cell resolution by tissue decolorization. *Cell* **159**, 911–924 (2014).
24. Belle, M. et al. Tridimensional visualization and analysis of early human development. *Cell* **169**, 161–173 (2017).
25. Lai, H. M. et al. Next generation histology methods for three-dimensional imaging of fresh and archival human brain tissues. *Nat. Commun.* **9**, 1066 (2018).
26. Hama, H. et al. ScaleS: an optical clearing palette for biological imaging. *Nat. Neurosci.* **18**, 1518–1529 (2015).
27. Gleave, J. A., Lerch, J. P., Henkelman, R. M. & Nieman, B. J. A method for 3D immunostaining and optical imaging of the mouse brain demonstrated in neural progenitor cells. *PLoS ONE* **8**, e72039 (2013).
28. Sillitoe, R. V. & Hawkes, R. Whole-mount immunohistochemistry: a high-throughput screen for patterning defects in the mouse cerebellum. *J. Histochem. Cytochem.* **50**, 235–244 (2002).
29. Dent, J. A., Polson, A. G. & Klymkowsky, M. W. A whole-mount immunocytochemical analysis of the expression of the intermediate filament protein vimentin in *Xenopus*. *Development* **105**, 61–74 (1989).
30. Mai, H. et al. Whole-body cellular mapping in mouse using standard IgG antibodies. *Nat. Biotechnol.* **42**, 617–627 (2023).
31. Kubota, S. I. et al. Whole-body profiling of cancer metastasis with single-cell resolution. *Cell Rep.* **20**, 236–250 (2017).
32. Li, W., Germain, R. N. & Gerner, M. Y. Multiplex, quantitative cellular analysis in large tissue volumes with clearing-enhanced 3D microscopy (Ce3D). *Proc. Natl Acad. Sci. USA* **114**, E7321–E7330 (2017).
33. Dean, K. M., Roudot, P., Welf, E. S., Danuser, G. & Fiolka, R. Deconvolution-free subcellular imaging with axially swept light sheet microscopy. *Biophys. J.* **108**, 2807–2815 (2015).
34. Shi, L. et al. Highly-multiplexed volumetric mapping with Raman dye imaging and tissue clearing. *Nat. Biotechnol.* **40**, 364–373 (2021).
35. Kim, S.-Y. et al. Stochastic electrotransport selectively enhances the transport of highly electromobile molecules. *Proc. Natl Acad. Sci. USA* **112**, E6274–E6283 (2015).
36. Pavlova, I. P., Shipley, S. C., Lanio, M., Hen, R. & Denny, C. A. Optimization of immunolabeling and clearing techniques for indelibly-labeled memory traces. *Hippocampus* **28**, 523–535 (2018).
37. Yau, C. N. et al. Principles of deep immunohistochemistry for 3D histology. *Cell Rep. Methods* **3**, 100458 (2023).
38. Murakami, T. C. et al. A three-dimensional single-cell-resolution whole-brain atlas using CUBIC-X expansion microscopy and tissue clearing. *Nat. Neurosci.* **21**, 625–637 (2018).
39. Roberts, D. et al. Specific ion and buffer effects on protein–protein interactions of a monoclonal antibody. *Mol. Pharm.* **12**, 179–193 (2015).
40. Qualtiere, L. F., Anderson, A. G. & Meyers, P. Effects of ionic and nonionic detergents on antigen-antibody reactions. *J. Immunol.* **119**, 1645–1651 (1977).
41. Cabral, D. J., Hamilton, J. A. & Small, D. M. The ionization behavior of bile acids in different aqueous environments. *J. Lipid Res.* **27**, 334–343 (1987).
42. Esposito, G., Giglio, E., Pavel, N. V. & Zanobi, A. Size and shape of sodium deoxycholate micellar aggregates. *J. Phys. Chem.* **91**, 356–362 (1987).

43. Makino, S., Reynolds, J. A. & Tanford, C. The binding of deoxycholate and Triton X 100 to proteins. *J. Biol. Chem.* **248**, 4926–4932 (1973).
44. Proença, L. et al. Electrocatalytic oxidation of D-sorbitol on platinum in acid medium: analysis of the reaction products. *J. Electroanal. Chem.* **432**, 237–242 (1997).
45. Albanese, A. et al. Multiscale 3D phenotyping of human cerebral organoids. *Sci. Rep.* **10**, 21487 (2020).
46. Roy, D. S. et al. Brain-wide mapping reveals that engrams for a single memory are distributed across multiple brain regions. *Nat. Commun.* **13**, 1799 (2022).
47. Muzumdar, M. D., Tasic, B., Miyamichi, K., Li, L. & Luo, L. A global double-fluorescent Cre reporter mouse. *Genesis* **45**, 593–605 (2007).
48. Livet, J. et al. Transgenic strategies for combinatorial expression of fluorescent proteins in the nervous system. *Nature* **450**, 56–62 (2007).
49. Gong, S. et al. A gene expression atlas of the central nervous system based on bacterial artificial chromosomes. *Nature* **425**, 917–925 (2003).
50. Valjent, E., Bertran-Gonzalez, J., Hervé, D., Fisone, G. & Girault, J.-A. Looking BAC at striatal signaling: cell-specific analysis in new transgenic mice. *Trends Neurosci.* **32**, 538–547 (2009).
51. Kim, Y. et al. Brain-wide maps reveal stereotyped cell-type-based cortical architecture and subcortical sexual dimorphism. *Cell* **171**, 456–469 (2017).
52. Zhang, C. et al. A platform for stereological quantitative analysis of the brain-wide distribution of type-specific neurons. *Sci. Rep.* **7**, 14334 (2017).
53. Tanahira, C. et al. Parvalbumin neurons in the forebrain as revealed by parvalbumin-Cre transgenic mice. *Neurosci. Res.* **63**, 213–223 (2009).
54. Nigro, M. J., Kirikae, H., Kjelsberg, K., Nair, R. R. & Witter, M. P. Not all that is gold glitters: PV-IRES-Cre mouse line shows low efficiency of labeling of parvalbumin interneurons in the perirhinal cortex. *Front. Neural Circuits* **15**, 781928 (2021).
55. Li, X. et al. Generation of a whole-brain atlas for the cholinergic system and mesoscopic projectome analysis of basal forebrain cholinergic neurons. *Proc. Natl Acad. Sci. USA* **115**, 415–420 (2018).
56. Heffner, C. S. et al. Supporting conditional mouse mutagenesis with a comprehensive cre characterization resource. *Nat. Commun.* **3**, 1218 (2012).
57. von Engelhardt, J., Eliava, M., Meyer, A. H., Rozov, A. & Monyer, H. Functional characterization of intrinsic cholinergic interneurons in the cortex. *J. Neurosci.* **27**, 5633–5642 (2007).
58. Vogel, C. & Marcotte, E. M. Insights into the regulation of protein abundance from proteomic and transcriptomic analyses. *Nat. Rev. Genet.* **13**, 227–232 (2012).
59. Madisen, L. et al. A robust and high-throughput Cre reporting and characterization system for the whole mouse brain. *Nat. Neurosci.* **13**, 133–140 (2009).
60. Luo, L. et al. Optimizing nervous system-specific gene targeting with Cre driver lines: prevalence of germline recombination and influencing factors. *Neuron* **106**, 37–65 (2020).
61. Swaney, J. et al. Scalable image processing techniques for quantitative analysis of volumetric biological images from light-sheet microscopy. Preprint at *bioRxiv* <https://doi.org/10.1101/576595> (2019).
62. Tallini, Y. N. et al. BAC transgenic mice express enhanced green fluorescent protein in central and peripheral cholinergic neurons. *Physiol. Genomics* **27**, 391–397 (2006).
63. Schmidt-Supprian, M. & Rajewsky, K. Vagaries of conditional gene targeting. *Nat. Immunol.* **8**, 665–668 (2007).
64. Matthaei, K. I. & Matthaei, K. I. Genetically manipulated mice: a powerful tool with unsuspected caveats. *J. Physiol.* **582**, 481–488 (2007).
65. Huang, Z. J., Taniguchi, H., He, M. & Kuhlman, S. Genetic labeling of neurons in mouse brain. *Cold Spring Harb. Protoc.* **2014**, 150–160 (2014).
66. Marin, O. Interneuron dysfunction in psychiatric disorders. *Nat. Rev. Neurosci.* **13**, 107–120 (2012).
67. Zikopoulos, B. & Barbas, H. Altered neural connectivity in excitatory and inhibitory cortical circuits in autism. *Front. Hum. Neurosci.* **7**, 609 (2013).
68. Niwa, M. et al. Knockdown of DISC1 by in utero gene transfer disturbs postnatal dopaminergic maturation in the frontal cortex and leads to adult behavioral deficits. *Neuron* **65**, 480–489 (2010).
69. Canty, A. J. et al. Regionalized loss of parvalbumin interneurons in the cerebral cortex of mice with deficits in GFR α 1 signaling. *J. Neurosci.* **29**, 10695–10705 (2009).
70. Park, J. et al. Integrated platform for multiscale molecular imaging and phenotyping of the human brain. *Science* **384**, eadh9979 (2024).
71. Caballero, A., Flores-Barrera, E., Cass, D. K. & Tseng, K. Y. Differential regulation of parvalbumin and calretinin interneurons in the prefrontal cortex during adolescence. *Brain Struct. Funct.* **219**, 395–406 (2014).
72. Caballero, A., Flores-Barrera, E., Thomases, D. R. & Tseng, K. Y. Downregulation of parvalbumin expression in the prefrontal cortex during adolescence causes enduring prefrontal disinhibition in adulthood. *Neuropsychopharmacology* **45**, 1527–1535 (2020).
73. Black, S. et al. CODEX multiplexed tissue imaging with DNA-conjugated antibodies. *Nat. Protoc.* **16**, 3802–3835 (2021).
74. Hong, F. et al. Thermal-plex: fluidic-free, rapid sequential multiplexed imaging with DNA-encoded thermal channels. *Nat. Methods* **21**, 331–341 (2023).

Publisher's note Springer Nature remains neutral with regard to jurisdictional claims in published maps and institutional affiliations.

Springer Nature or its licensor (e.g. a society or other partner) holds exclusive rights to this article under a publishing agreement with the author(s) or other rightsholder(s); author self-archiving of the accepted manuscript version of this article is solely governed by the terms of such publishing agreement and applicable law.

© The Author(s), under exclusive licence to Springer Nature America, Inc. 2025

Methods

Mice

Young adult (2–4 months old) C57BL/6 mice were housed in a 12-h light/dark cycle, 18–23 °C ambient temperature and 40–60% ambient humidity with unrestricted access to food and water. All experimental protocols were approved by the Massachusetts Institute of Technology (MIT) Institutional Animal Care and Use Committee and the Division of Comparative Medicine and were in accordance with guidelines from the National Institutes of Health (NIH). The following transgenic lines were used for this study: ChAT^{BAC}-eGFP (Jackson, stock no. 007902) and PV-Cre/loxP-tdTomato double hemizygous (B6 Pvalb-IRES-Cre, Jackson, strain no. 017320, and Ai14, Jackson, strain no. 007914). For LPZ validation, paraformaldehyde (PFA)-perfused brains of young adult (8–10 weeks old) mice were sourced from the University of California, San Diego (UCSD) and Hilltop Lab Animals, Inc.

Rat

PFA-perfused whole brains of CVF Sprague-Dawley rat weanlings were purchased from Hilltop Lab Animals, Inc.

Marmoset

All animal experiments were approved by the MIT Institutional Animal Care and Use Committee and were performed under guidelines from the NIH. Adult common marmosets (2–4 years old) were housed in Association for Assessment and Accreditation of Laboratory Animal Care (AAALAC)-accredited facilities. The housing room was maintained at 74.0 ± 2.0 °F (23.3 ± 1.1 °C) in the relative humidity of 50 ± 20% and in a 12-h light/dark cycle. The animals were housed in dedicated cages with enrichment devices and had unrestricted access to food and water. For histological examinations, the animals were deeply sedated by intramuscular injection of ketamine (20–40 mg kg⁻¹) or alfaxalone (5–10 mg kg⁻¹), followed by intravenous injection of sodium pentobarbital (10–30 mg kg⁻¹). When pedal withdrawal reflex was eliminated and/or respiratory rate was diminished, animals were perfused transcardially with 0.5 ml of 1,000 IU ml⁻¹ heparin and 100–200 ml of cold PBS by gravity. Then, the descending aorta of the animals was clamped, and a peristaltic pump was used to infuse another 200–300 ml of ice-cold SHIELD perfusion solution (10% (w/v) GE38 and 4% PFA (w/v) in PBS). Brains were removed from the skulls and SHIELD processed (see the ‘SHIELD processing’ subsection).

Organoids

Organoids were grown according to the protocol by Lancaster et al.⁷⁵, with the addition of dual SMAD inhibition between day 6 and day 9 to increase neural differentiation as previously described⁷⁶. Organoids were grown from induced pluripotent stem cells (iPSCs) (System Biosciences, SC101A-1). After Matrigel droplet embedding, organoids were transferred to 60-mm suspension culture dishes (Corning, 430589) and placed on a shaker at 75 r.p.m. on day 16. The organoids were SHIELD processed on day 35 (see the ‘SHIELD processing’ subsection).

Human tissues

Banked human brain tissue samples in formalin solution were obtained from Massachusetts General Hospital. The brains were collected and banked in accordance with approval from the local institutional review board. The formalin solution was replaced with 1× PBSN made with modified 10× PBS solution, pH 7.2, and 0.02% sodium azide upon arrival, and the hemispheres were stored at 4 °C until use. Samples were SHIELD processed before delipidation and labeling (see the ‘SHIELD processing’ subsection).

Chemicals

List of chemicals used for this study and their sources unless otherwise specified: polyglycerol 3-polyglycidyl ether (CVC Thermoset Specialties of Emerald Performance Materials, GE38 or P3PE); 4%

paraformaldehyde (Electron Microscopy Sciences, 15714-S); sodium phosphate buffer (PB; Teknova, P2072); sodium chloride (Teknova, S5845); sodium carbonate (MilliporeSigma, S7795); sodium bicarbonate (MilliporeSigma, S5761); sodium dodecyl sulfate (SDS; MilliporeSigma, 75746); Triton X-100 (MilliporeSigma); sodium azide (MilliporeSigma, S2002); Trizma base (MilliporeSigma, T1503); NaDC (MilliporeSigma, D6750); and D-sorbitol (MilliporeSigma, S1876).

NaDC concentration measurement

The concentration of surfactants can be measured by the degree of solubilization of hydrophobic organic dyes. Above the critical micelle concentration, the amount of solubilized dye increases linearly with the increase in surfactant concentration⁷⁷. Degree of solubilization was measured based on light absorption using a spectrophotometer (Azzota, SM1100 Economic UV-VIS spectrophotometer) at 592 nm. Sufficient Sudan II dye (Sigma-Aldrich, 199656, powder) was added to fully saturate pure acetone at room temperature. Next, 200 µl of saturated solution was added to each 1.5-ml Eppendorf tube and then allowed to fully evaporate to deposit Sudan II dye to the well surface. This coating exceeds the dissolving capacity of 1 ml of aqueous solution. Five milliliters of eFLASH buffer was collected at various timepoints from multiple independent experiments (*n* = 6). One milliliter of each sample was added to the dye-coated 1.5-ml tubes and then incubated at 60 °C for 1 h and then at room temperature overnight while shaking. Then, 700 µl from each sample was pipetted into a cuvette, and absorbance values were recoded using a spectrophotometer. NaDC concentration was calculated based on a standard curve generated using the method described above from solutions with known concentrations of NaDC (Extended Data Fig. 2e).

SHIELD processing

Preservation of mouse brain hemispheres was carried out according to the previously published SHIELD protocol¹². Mice were transcardially perfused with ice-cold PBS and then with the SHIELD perfusion solution. Dissected brains or organs were incubated in the same perfusion solution at 4 °C for 48 h. Tissues were then transferred to the SHIELD-OFF solution (1× PBS containing 10% (w/v) P3PE) and incubated at 4 °C for 24 h. In the case of brain hemisphere processing, a whole brain was split into hemispheres before being incubated in the SHIELD-OFF solution. After the SHIELD-OFF step, the organs were placed in the SHIELD-ON solution (0.1 M sodium carbonate buffer at pH 10) and incubated at 37 °C for 24 h.

For whole mouse brains and whole rat brains received as already PFA fixed, they were post-fixed with SHIELD instead. PFA-fixed tissues incubated in SHIELD-OFF solution at 4 °C for 4–5 d with one exchange of fresh SHIELD-OFF solution halfway through; afterwards, the brains were incubated in SHIELD-ON solution at room temperature for 24 h. Processed samples were washed in PBS for at least 24 h with multiple solution exchanges.

Marmoset brains perfused with ice-cold PBS and then with SHIELD perfusion solution were incubated in the same perfusion solution at 4 °C for 48 h. The brain was hemisected, transferred to the SHIELD-OFF solution and incubated at 4 °C for 24 h. After the SHIELD-OFF step, the hemispheres were incubated in the SHIELD-ON solution at 37 °C for 24 h. Afterwards, the hemispheres were transferred to PBS for washing.

Formalin-fixed human tissues were obtained from the Massachusetts General Hospital brain tank. The 4-mm-thick coronal slabs were incubated in the SHIELD-OFF solution for 48 h. After the SHIELD-OFF step, the tissues are incubated in the SHIELD-ON solution at 37 °C.

Organoids were fixed in 1× PBS with 4% (w/v) PFA at room temperature for 30 min and subsequently incubated in SHIELD-OFF solution at 4 °C for 48 h. Samples were then incubated in SHIELD-ON solution at 37 °C overnight before washing with PBS with 0.02% sodium azide at room temperature for at least 24 h.

Passive clearing (delipidation)

SHIELD-processed samples were delipidated before labeling or imaging. Passive delipidation was done by incubating tissues in the clearing buffer (300 mM SDS, 10 mM sodium borate, 100 mM sodium sulfite, pH 9.0). Thin slices between 100- μ m and 200- μ m thickness were cleared at 45 °C clearing buffer for 2–3 h. Mouse brain hemispheres were cleared at 45 °C for 10–14 d. Organoids were cleared at 55 °C for 36 h. Human tissue slab was cleared at 80 °C until translucent for approximately 1 week.

Active clearing (SE)

SHIELD-processed samples can also be cleared rapidly using SE (LifeCanvas Technologies, SmartClear Pro). Mouse brain hemispheres were cleared at 45 °C for 3–4 d. Whole mouse brains were cleared for approximately 1 week. Whole rat brains were cleared for approximately 10 d. The marmoset brain hemisphere was cut coronally into four blocks of 8-mm thickness using a microtome, and the blocks were cleared for 2 weeks.

Antibody destaining

Samples previously labeled with antibodies were first incubated in fresh clearing buffer overnight at 37 °C. Afterwards, the samples were moved to 50 ml of pre-heated 80 °C clearing buffer on a heated shaker for 1 h, maintaining the temperature at 80 °C. Next, the samples were transferred to fresh room temperature clearing buffer and incubated overnight on a shaker at 37 °C. The sample was washed using PBS with multiple solution exchanges for 1 d to thoroughly wash out SDS. Only SHIELD-processed samples are compatible with this destaining protocol.

Passive immunohistochemistry

Immunohistochemistry was performed on 100- μ m-thick or 200- μ m-thick mouse or marmoset brain tissue sections. Staining was performed on 24-well or 48-well plates with primary antibodies (per recommended dilution from each vendors) and with dye-conjugated Fc-specific Fab secondary antibodies (1:3 molar ratio between Fab fragments and the primary antibody; Jackson ImmunoResearch) or dye-conjugated IgG secondary antibodies (1:2 molar ratio between full-size secondary antibody and primary antibody; Abcam) for 1 d at room temperature in PBS with 0.1% Triton X-100 (PBST). Similar protocols were used to characterize antibody binding performance in several different buffers: 50 mM Tris buffer with 0.1% NaDC, 50 mM Tris with 1% NaDC, eFLASH initial buffer and eFLASH terminal buffer (buffer retrieved from the eFLASH staining device after 24 h).

Immunohistochemistry for pH and NaDC effect characterization

For buffer characterization in Fig. 2a,b and Extended Data Fig. 3a, initial primary antibody staining of 100- μ m mouse tissue sections with anti-PV and anti-NPY was shortened to 2 h at 37 °C in experimental conditions: 50 mM Tris buffer with pH 7.5, pH 9 and pH 10, pH 7.5 with 0.1% NaDC, pH 7.5 with 1% NaDC and pH 10 with 1% NaDC. After brief washing in their respective buffers for 1 h and then in PBS for 1 h, samples are labeled with Alexa Fluor 647 secondary antibody for 4 h. After another round of washing for 4 h, samples were briefly fixed in 4% PFA in PBS for 1 h at 37 °C and then thoroughly washed with PBS overnight at room temperature. Finally, an additional round of normal immunohistochemistry was performed in PBST with additional primary antibodies and Alexa Fluor 488 secondary antibodies. Segmentation masks for soma intensity analysis were drawn based on Alexa Fluor 488 channel using ImageJ ($n = 3$ independent experiments for each condition). Total number of cells per condition, respectively, for anti-PV: 139, 97, 97, 101, 93 and 66. Total number of cells per condition, respectively, for anti-NPY: 43, 31, 21, 21, 23 and 21.

eFLASH protocol

Volumetric immunolabeling with eFLASH was carried out with a device described in Kim et al.³⁵. Experiments were carried out with two buffers. The main buffer (100 mM Tris, 4% (w/v) D-sorbitol, 0.1% (v/v) Triton X-100 and 0.1% (w/v) NaDC, titrated to pH 9.5 with formic acid) is a circulation solution that allows conduction of electricity. The sample buffer (100 mM Tris, 4% (w/v) D-sorbitol, 0.2% (v/v) Triton X-100 and 1% (w/v) NaDC, titrated to pH 9.5 with formic acid) is used to fill the sample cup along with the tissue and antibodies. Then, 350 ml of the main buffer was loaded into the staining device, and 2–10 ml of the sample buffer was loaded into the sample cup, adjusted based on the sample to fully submerge the sample. The tissue sample was placed in a nylon mesh and then placed into the sample cup to prevent direct contact with the nanoporous membrane of the sample cups. For one-shot labeling, primary antibodies and secondary Fc-specific Fab fragment antibodies were added to the sample cup at the sample time, 1:2 molar ratio. For separate labeling of primary and secondary antibodies (non-Fc-specific Fab fragment antibodies), two rounds of eFLASH labeling were performed back to back with washing in between. For secondary antibody labeling only, alternate buffers can be used for shorter 4–6-h experiments: 100 mM Tris, 0.1% (v/v) Triton X-100 and 0.1% (w/v) NaDC, titrated to pH 8 with formic acid for both main chamber (350 ml) and sample cup (2–10 ml). For a single round of eFLASH experiment, electric field was applied for 24 h at 90 V with maximum current limited to 500 mA. Temperature control was set to maintain 25 °C. Sample cup stir bar rotation was set to 850 r.p.m., and sample cup rotation speed was set to 0.01 r.p.m. Suggested amounts of primary antibodies for whole mouse brain-sized samples are included in Supplementary Table 1. Labeling conditions used for experiments shown on figures can be found in Supplementary Table 2.

Dye conjugation of secondary antibodies

For the far-red channel, secondary antibodies conjugated with SeTau647 were used for most labeling experiments as they provide superior photo-stability when compared to commercially available dyes⁷⁸. SeTau-647-NHS was purchased from SETA BioMedicals, and 10- μ l 10 mM aliquots were prepared using DMSO (Sigma-Aldrich, anhydrous, ZerO2, $\geq 99.9\%$). SeTau-647-NHS was reacted with non-conjugated Fc-specific Fab fragments at 10:1 ratio (Jackson ImmunoResearch) for 1 h at room temperature. Afterwards, the solution was purified using Zeba Spin Desalting Columns (7k molecular weight cutoff (MWCO), Thermo Fisher Scientific) 2–3 times until the desalting column ran clean. The concentration of the resulting solution was measured using DC Protein Assay (Bio-Rad) before use.

Refractive index matching

Optical clearing of delipidated samples was achieved using Protos-based immersion medium¹². For samples thicker than 1 mm, optical clearing was done in two steps. Labeled samples were first incubated in half-step solution (50/50 mix of 2 \times PBS and Protos-based immersion medium) at 37 °C overnight. Afterwards, the samples were moved to the pure immersion medium and incubated at 37 °C overnight.

Fixation of labeled samples

For antibodies that are not stable in Protos-based immersion medium, the eFLASH-labeled samples were fixed with 4% (w/v) PFA to prevent dissociation of bound antibodies. eFLASH-labeled samples were first washed in 1 \times PBS with 0.02% (w/v) sodium azide at room temperature for at least 6 h to wash out Tris. Samples were then moved to freshly prepared 4% (w/v) PFA solution in 1 \times PBS and placed on an orbital shaker at room temperature overnight. Samples were then washed with 1 \times PBS with 0.02% (w/v) sodium azide at room temperature with multiple solution exchanges for at least 6 h.

Lightsheet imaging and post-processing

Rapid volumetric imaging was performed with an axially swept lightsheet microscope (LifeCanvas Technologies, SmartSPIM) equipped with three lasers (488 nm, 561 nm and 642 nm). The microscope focus was fine-tuned for each sample by finely adjusting the position of the illumination objectives to ensure optimal optical sectioning. Focus compensation was programmed as a function of depth for each laser line to account for slight focal variations through imaging depth. All lightsheet imaging was done with either the $\times 3.6$ objective (custom LifeCanvas Technologies design, 0.2 numerical aperture (NA) 12-mm working distance (WD), lateral resolution 1.8 μm in x - y) and the $\times 10$ objective (Olympus, XLPLN10XSVM, 0.6 NA, 8-mm WD, lateral resolution 0.66 μm in x - y). Acquired data were post-processed with algorithms described in Swaney et al.⁶¹. A complete table of imaging modalities and conditions for all data included in this paper can be found in Supplementary Table 3. For visualization, Imaris (Bitplane) and ImageJ were used.

Volumetric cell detection

Detection of cells was accomplished by blob detection, followed by dimensionality reduction and classification. Blobs were detected by computing the difference of Gaussians followed by identification of voxels that were the maximum of their neighbors within a chosen radius. Then, 31×31 pixel patches were extracted in the x - y , x - z and y - z planes. The raster of these patches was concatenated, and the three resulting 961-element vectors were concatenated to create a 2,883-feature vector. All patches of putative cell centers within the volume were collected, and principal component analysis (PCA) was performed to reduce the dimensionality of the vector to 48 components. Each of these components was composed of 2,883 elements, which were multiplied with the 2,883-feature vector per patch to produce 48 numerical features. The vector of each component can be visualized as three 31×31 planes to allow interpretation of the magnitude of the component. The 48 numerical features were then used to train a random forest classifier using iterative user-supervised training. Finally, the classifier was applied to all patches in the volume to classify each local maximum as a positive cell detection or a negative artifact detection.

Atlas alignment

Atlas alignments of mouse brain hemispheres labeled with eFLASH to the Allen brain reference atlas, CCF V3 (ref. 79), were carried out using the hybrid automated atlas alignment method described in Swaney et al.⁶¹, which combines Elastix⁸⁰ and manual refinement tools to improve alignment accuracy.

Brain region segmentation

Detected cell coordinates were transformed from the original coordinate space to the reference coordinate after atlas alignment. The alignment was used to construct a 3D radial basis function using thin-plate splines to map points in the original coordinate space to the reference coordinate space. The point locations in the reference space were then matched against the Allen Brain Mouse Atlas⁷⁹ reference segmentation to yield counts per brain region. These counts were then used to color the regions in the Allen Brain Mouse Atlas coronal SVG image files. Calculations and visualizations were done using the Nuggt Python package⁶¹.

Statistics and reproducibility

The numbers of independent experiments performed for this study with similar results are noted in this section regarding Figs. 3a–f and 4a,b,d,e,g,h and Extended Data Figs. 3a–g, 4a–q and 5a,b,d,e,g,h. The numbers of independent volumetric labeling experiments with eFLASH for each antibody are as follows: anti-NeuN (Cell Signaling Technology (CST), 24307: mouse brain 19; rat brain 1); anti-PV (Invitrogen, PA1-933: mouse brain 74; marmoset brain block 2); anti-TH (BioLegend, 818001: mouse brain 27; mouse heart 2); anti-ChAT

(Millipore, AB144P: mouse brain 22); anti-NPY (CST, 11976: mouse brain 41; marmoset brain block 2; human brain block 1); anti-Ret (R&D Systems, AF482: mouse embryo 1); anti-NF-M (Encor, MCA-3H11: mouse embryo 1; mouse brain 1); anti-vimentin (CST, 9856S: organoid 4); anti- β -tubulin (BioLegend, 801208: organoid 4, BioLegend, 801201: mouse intestine 1); anti-histone-H3 (Abcam, ab237418: mouse liver lobule 1); anti- α -SMA (Millipore, C6198: mouse lung 1; mouse heart 2); anti-myosin7a (Proteus, 25-6790: mouse ear canal 1); anti-CB (CST, 13176: mouse brain 21); anti-VIP (Abcam, ab227850: mouse brain 8); anti-SST (Santa Cruz Biotechnology, sc-47706: mouse brain 11); anti-nNOS (Abcam, ab1376: mouse brain 2); anti-Iba1 (CST, 17198: mouse brain 36); anti-GFAP (BioLegend, 644708: mouse brain 10); anti-TPH2 (Invitrogen, PA1-778: mouse brain 5); anti-c-Fos (Abcam, ab214672: mouse brain 9); anti-NF(SMI312) (BioLegend, 837904: mouse brain 9); and anti-calretinin (Abcam, ab702: mouse brain 8).

Reporting summary

Further information on research design is available in the Nature Portfolio Reporting Summary linked to this article.

Data availability

All data supporting the findings of this study, including computational modeling data and primary image volumes, are available from the corresponding author upon reasonable request.

Code availability

Code used for this study can be found in the following public GitHub repository: <https://github.com/chunglabmit/eflash> (ref. 81).

References

- Lancaster, M. A. & Knoblich, J. A. Generation of cerebral organoids from human pluripotent stem cells. *Nat. Protoc.* **9**, 2329–2340 (2014).
- Mellios, N. et al. MeCP2-regulated miRNAs control early human neurogenesis through differential effects on ERK and AKT signaling. *Mol. Psychiatry* **23**, 1051–1065 (2017).
- Tehrani-Bagha, A. R. & Holmberg, K. Solubilization of hydrophobic dyes in surfactant solutions. *Materials* **6**, 580–608 (2013).
- Podgorski, K., Terpetschnig, E., Klochko, O. P., Obukhova, O. M. & Haas, K. Ultra-bright and -stable red and near-infrared squaraine fluorophores for in vivo two-photon imaging. *PLoS ONE* **7**, e51980 (2012).
- Dong, H. W. *Allen Reference Atlas: A Digital Color Brain Atlas of the C57Bl/6J Male Mouse* (Wiley, 2008).
- Klein, S., Staring, M., Murphy, K., Viergever, M. A. & Pluim, J. elastix: a toolbox for intensity-based medical image registration. *IEEE Trans. Med. Imaging* **29**, 196–205 (2010).
- Yun, D. H. et al. Uniform volumetric single-cell processing for organ-scale molecular phenotyping. *GitHub* <https://github.com/chunglabmit/eflash> (2024).

Acknowledgements

The authors thank the entire Chung laboratory for support and discussions. We acknowledge N. Peat for contribution to chemical screening for buffer development, L. Ochoa for discussions on transgenic mouse lines and J. Zeng for experimental support. K.C. was supported by the Burroughs Wellcome Fund Career Awards at the Scientific Interface; the Searle Scholars Program; the Packard Award in Science and Engineering; the NARSAD Young Investigator Award; and the McKnight Foundation Technology Award. K.C. and this work were supported by the JPB Foundation (PIIF and PNDRF), the NCSOFT Cultural Foundation and the National Institutes of Health (1-DP2-ESO27992 and U01MH117072). J.P. was supported by postdoctoral fellowships from the Picower Institute of Learning and Memory.

Author contributions

D.H.Y., Y.-G.P. and K.C. ideated the concept of CuRVE, designed the experiments and wrote the manuscript, with input from other authors. D.H.Y. and K.C. designed eFLASH protocols and systems, with help from J.H.C. on the initial prototype. D.H.Y. performed the volumetric tissue clearing and labeling, with assistance from N.D. Y.-G.P. aided the development of the eFLASH technology by performing passive staining experiments for screening antibodies and buffers and imaging eFLASH-labeled samples. Y.-G.P. led SHIELD processing of all tissue samples, with help from K.X. and J.P. G.F. and K.C. initiated the marmoset brain mapping project. G.F. provided the marmoset, and Q.Z. perfused the marmoset. L.K., M.E.K. and J.S. developed the computational pipeline, with input from Y.-G.P., D.H.Y., W.G. and K.C. N.B.E. and Y.-G.P. performed lightsheet imaging, with help from H.C. D.H.Y. performed the computational modeling in Fig. 1, with assistance from S.W.C. D.H.Y. performed the buffer characterization in Fig. 2. A.A. provided and imaged the SHIELD-processed cerebral organoid for Fig. 3. Y.-G.P. and L.K. performed brain-wide cell type mapping in Fig. 4, with help from D.H.Y. and K.X. Y.-G.P. performed cell detection and LPZ analysis in Fig. 5. C.H.S. aided in antibody and fluorescent dye screening for the project. G.D. and Y.T. helped with initial manuscript preparation. Y.T. and L.R. aided in detergent and buffer screening and characterization, including antibody electromobility measurements.

Competing interests

K.C. and J.H.C. are co-inventors on patents owned by MIT covering the SE technology. K.C. is a co-founder of LifeCanvas Technologies, a startup that provides solutions for 3D tissue processing and analysis. The other authors declare no competing interests.

Additional information

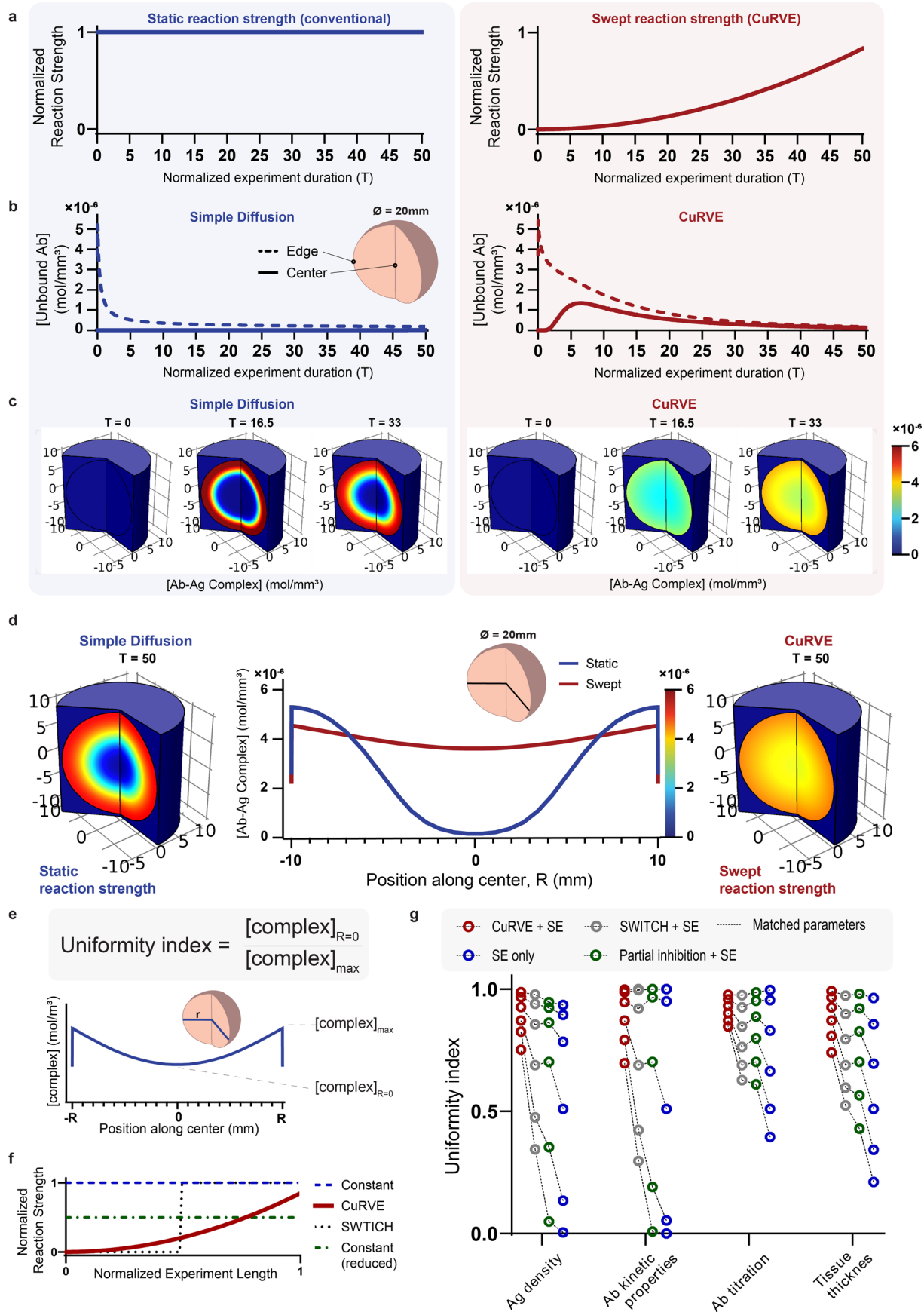
Extended data is available for this paper at <https://doi.org/10.1038/s41587-024-02533-4>.

Supplementary information The online version contains supplementary material available at <https://doi.org/10.1038/s41587-024-02533-4>.

Correspondence and requests for materials should be addressed to Kwanghun Chung.

Peer review information *Nature Biotechnology* thanks the anonymous reviewers for their contribution to the peer review of this work.

Reprints and permissions information is available at www.nature.com/reprints.

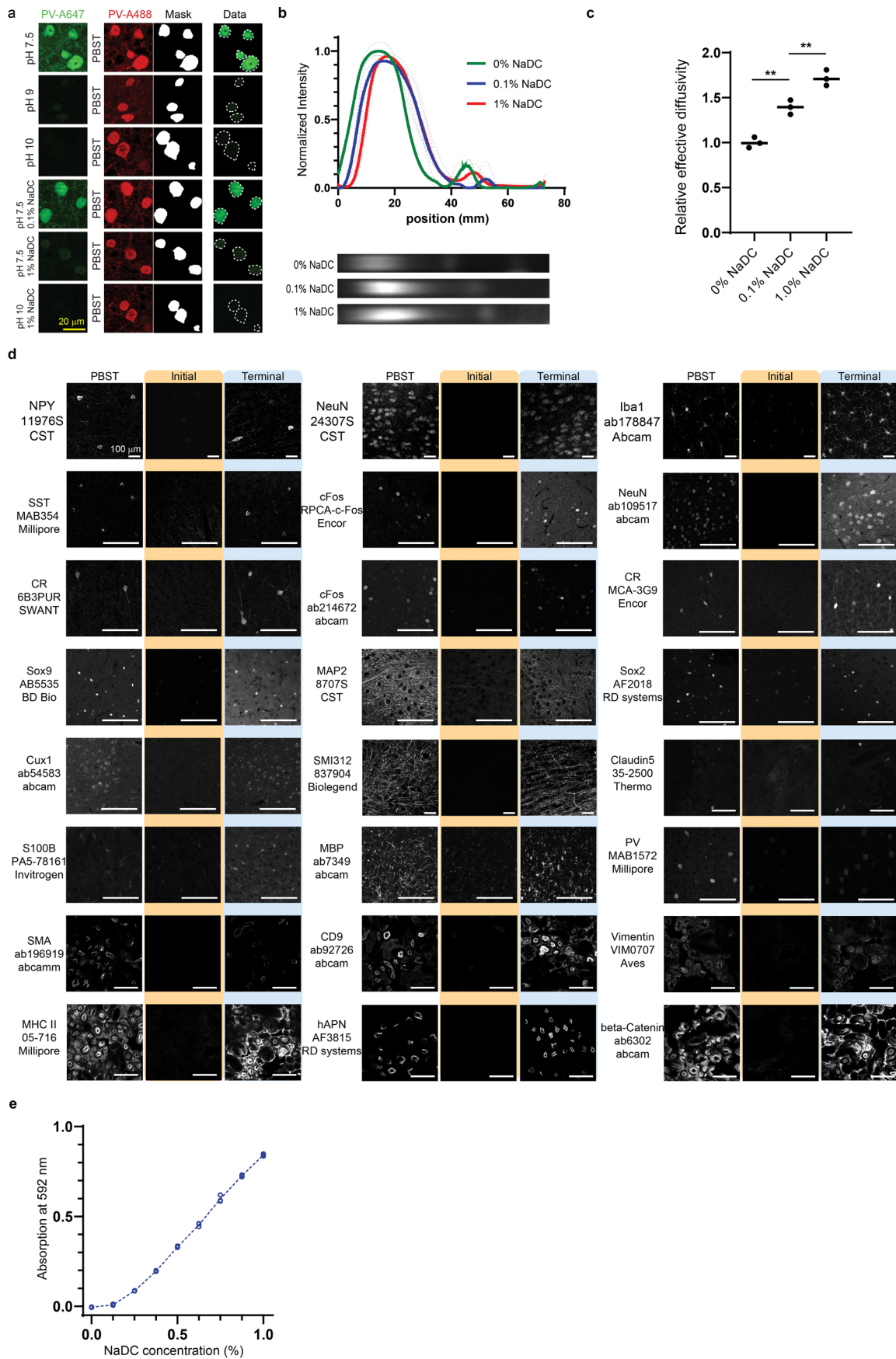


Extended Data Fig. 1 | See next page for caption.

Extended Data Fig. 1 | Extended computational modeling of CuRVE.

(a-c) Computational modeling of CuRVE in COMSOL for volumetric immunolabeling with simple diffusion. Model for conventional constant reaction methodology, static binding strength (left, blue line). Model for CuRVE, swept binding strength (right, red line). (a) Normalized reaction strength modulation through time. Note that the experimental duration is normalized to simulations on Fig. 1c-g, which share identical parameters except the reaction rate and effective diffusivity. (b) Concentration of unbound antibodies evaluated near the surface (dotted line) and the center (solid line) throughout the simulation duration. Static, simple diffusion (left), Swept, CuRVE (right). (c) Concentration of antibody-antigen complexes throughout the volume represented by a color heatmap. Time points rendered: $T=0, 16.5, 33$ for both simulations. (d) Overlaid concentration profiles of antibody-antigen complexes through the center of the volume at the end of the simulation. Volume rendering of the simple diffusion model (left), and the CuRVE model (right). (e-g) Sensitivity analysis

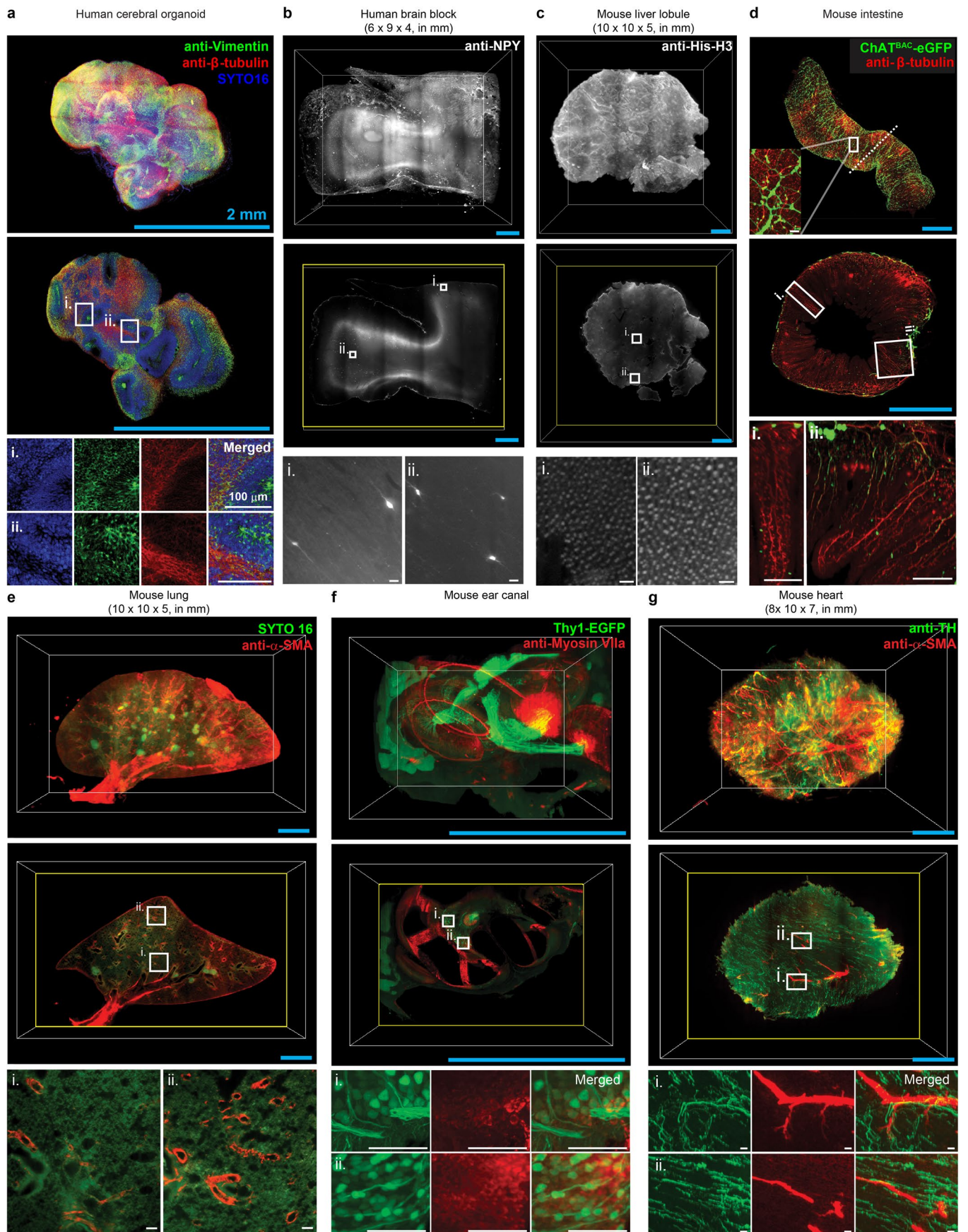
of CuRVE, SWITCH, and constant reaction scenarios. (e) The uniformity index represents the flatness of the Ag-Ab complex concentration profile given by concentration at center divided by maximum concentration. (f) Normalized reaction strength profile throughout the experiment: CuRVE (red), SWITCH (black), constant reaction (reduced rate) (green), and constant reaction (blue). (g) Sensitivity analysis through parametric sweep of four different variables. Tissue antigen density variability: $4.74e-10, 1.5e-9, 4.74e-9, 1.5e-8, 4.74e-8, 1.5e-7$ [mol/L]. Equilibrium dissociation constant variability (that is, antibody kinetic properties): $1e-7, 1e-8, 1e-9, 1e-10, 1e-11, 1e-12$ [mol/L]. Antibody titration variability (that is, antibody to antigen molar ratio): 0.1, 0.3, 0.5, 0.7, 0.9, 1.1. Tissue thickness variability: 5, 10, 15, 20, 25, 30 [mm]. CuRVE + SE (red circle). SWITCH + SE (grey circle). Partial inhibition + SE (green circle). SE only (blue circle). Data points evaluated with matching parameters are linked via dotted lines.



Extended Data Fig. 2 | See next page for caption.

Extended Data Fig. 2 | Validation of antibody binding modulation for volumetric immunolabeling. (a) Representative microscopy images and segmentation masks generated for quantification of the effect of pH and NaDC concentration on antibody binding. Initial labeling conducted in respective buffers with Alexa 647 secondary (green) and additional labeling conducted with additional primary antibody and Alexa 488 secondary (red) for getting accurate soma masks. Scale bar = 20 μ m (yellow). (b-c) Representative images and quantification of antibody displacement under electrophoresis in buffer containing 0% (green), 0.1% (blue), and 1% (red) NaDC respectively. Solid lines show the average normalized fluorescent intensities along the gel length.

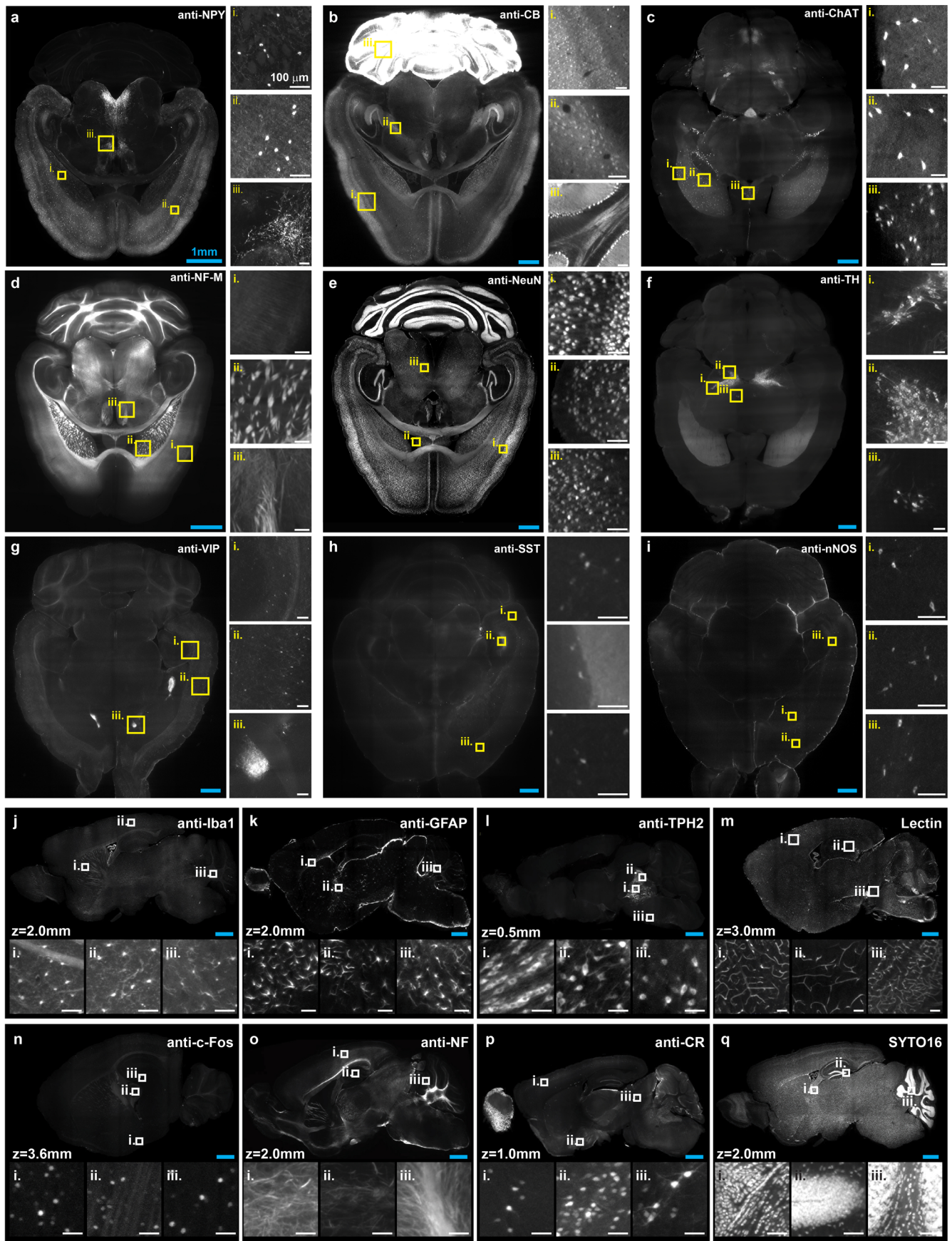
Individual data shown in lighter dotted lines. (c) Relative effective diffusivity of data in b calculated and normalized to 0% NaDC based on centroid of area under the curve. $N = 3$ independent experiments. One-Way ANOVA multiple comparisons, $**P = 0.0014$ (0% NaDC vs. 0.1% NaDC), $**P = 0.0040$ (0.1% NaDC vs. 1.0% NaDC). Mean and individual data shown. (d) Representative images of 24 antibodies labeled in PBST, initial state of eFLASH buffer (that is, antibody binding inhibitive state), and terminal state of eFLASH buffer (that is, nominal state). Scale bar = 100 μ m (white). (e) Calibration curve for spectrographic absorption of Sudan II dye at 592 nm for measuring NaDC concentration. $N = 3$ independent experiments for each condition.



Extended Data Fig. 3 | See next page for caption.

Extended Data Fig. 3 | Volumetric immunolabeling of various mammalian organs and organoids using eFLASH. (a-g) Whole volume rendering and representative optical plane image followed by magnified images. (a) Human iPS-derived cerebral organoid immunolabeled with anti-Vimentin (green), anti- β -tubulin (red), and SYTO 16. (a-i-ii) Magnified images of neuroepithelial formation around putative ventricles. (b) Human brain block containing grey and white matter regions immunolabeled with anti-NPY (white). (b-i-ii) Magnified images deep inside the white matter region. (c) Mouse liver lobule immunolabeled with anti-Histone-H3 (white). (c-i-ii) magnified images near the surface and the center regions. (d) Intestine section of ChAT^{BAC}-eGFP

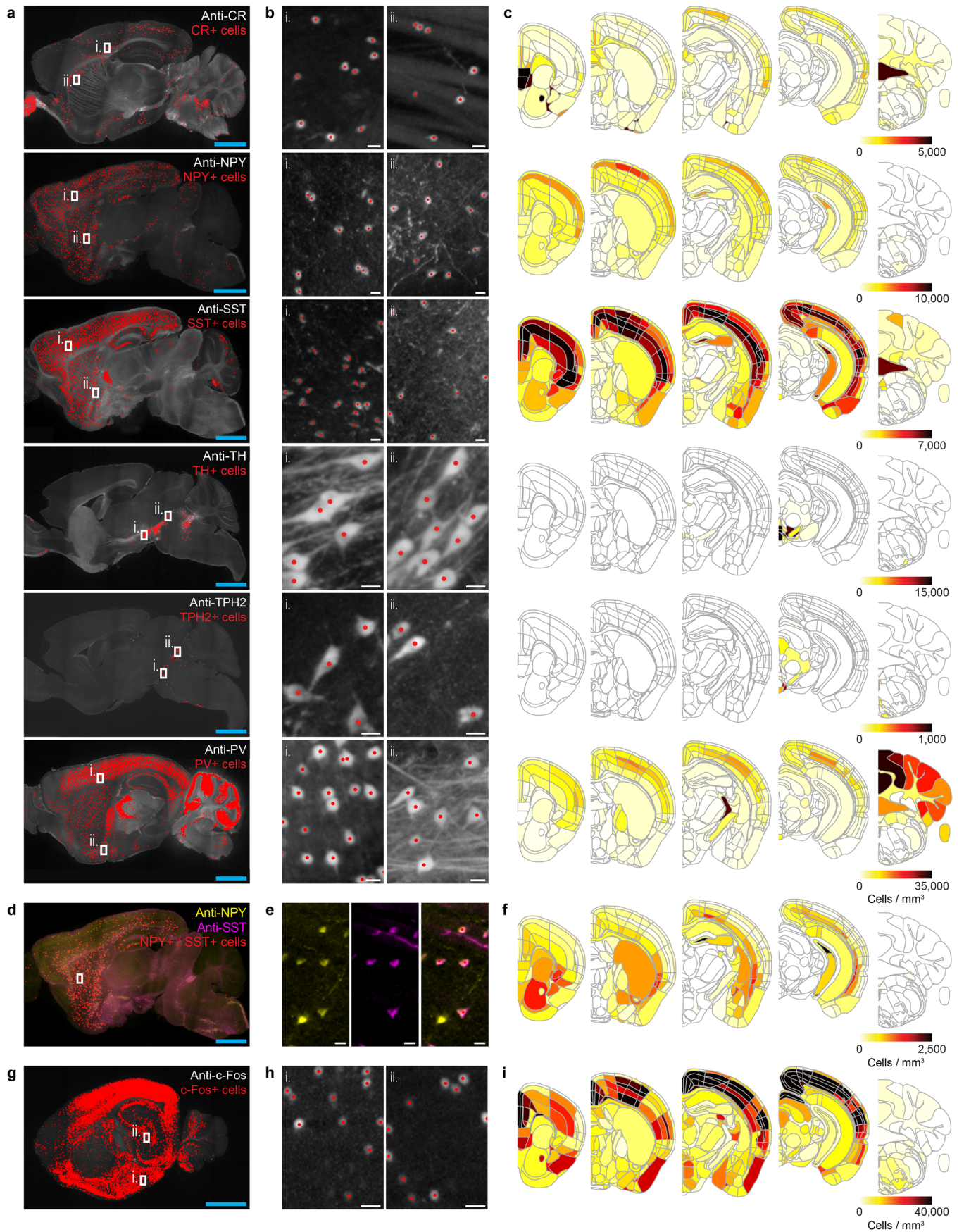
(green) transgenic mouse immunolabeled anti- β -tubulin (red). (d-i-ii) Magnified images of the villi structures. (e) Mouse lung immunolabeled with anti- α -SMA (red) and SYTO16. (e-i-ii) Magnified images of the airways accompanied by pulmonary and intraacinar arteries. (f) Ear canal of Thy1-EGFP (green) transgenic mouse immunolabeled with anti-Myosin VIIa (red) (f-i-ii) Magnified images of stereocilia and surrounding actin-based motor structures. (g) Mouse heart immunolabeled with anti-TH (green) and anti- α -SMA (red). (g-i-ii) Magnified images of dopaminergic innervations and actin filaments. Scale bars = 2 mm (cyan), 100 μ m (white).



Extended Data Fig. 4 | See next page for caption.

Extended Data Fig. 4 | Volumetric immunolabeling of mouse brains with various cell-type markers using eFLASH. (a–q) Representative optical plane from 3D imaging data (top), 20 mm MIP (middle), and (i–iii) magnified images (bottom): (a) anti-neuropeptide Y (NPY), neuronal marker, (b) anti-calbindin (CB), neuronal marker, (c) anti-choline acetyltransferase (ChAT), cholinergic neuronal marker, (d) anti-neurofilament-M (NF-M), neuronal structural marker, (e) anti-neuronal nuclei (NeuN), pan-neuronal marker, (f) anti-tyrosine hydroxylase (TH), dopaminergic neuronal marker, (g) anti-vasoactive intestinal peptide (VIP), neuroendocrine marker, (h) anti-somatostatin (SST), GABAergic

interneuron marker, (i) anti-neuronal nitric oxide synthases (nNOS), GABAergic interneuron marker, (j) anti-ionized calcium binding adaptor molecule (iba1), microglial and macrophage marker, (k) anti-glial fibrillary acidic protein (GFAP), astrocyte and neural stem cell marker (l) anti-tryptophan hydroxylase 2 (TPH2), serotonergic neuronal marker, (m) tomato lectin, vasculature stain, (n) anti-c-FOS, neuronal activity marker, (o) anti-neurofilament marker SMI-312 (anti-NF), pan-axonal marker, (p) anti-calretinin (CR), and (q) SYTO 16, nucleic acid stain. Scale bars = 1 mm (cyan), 100 μm (white).

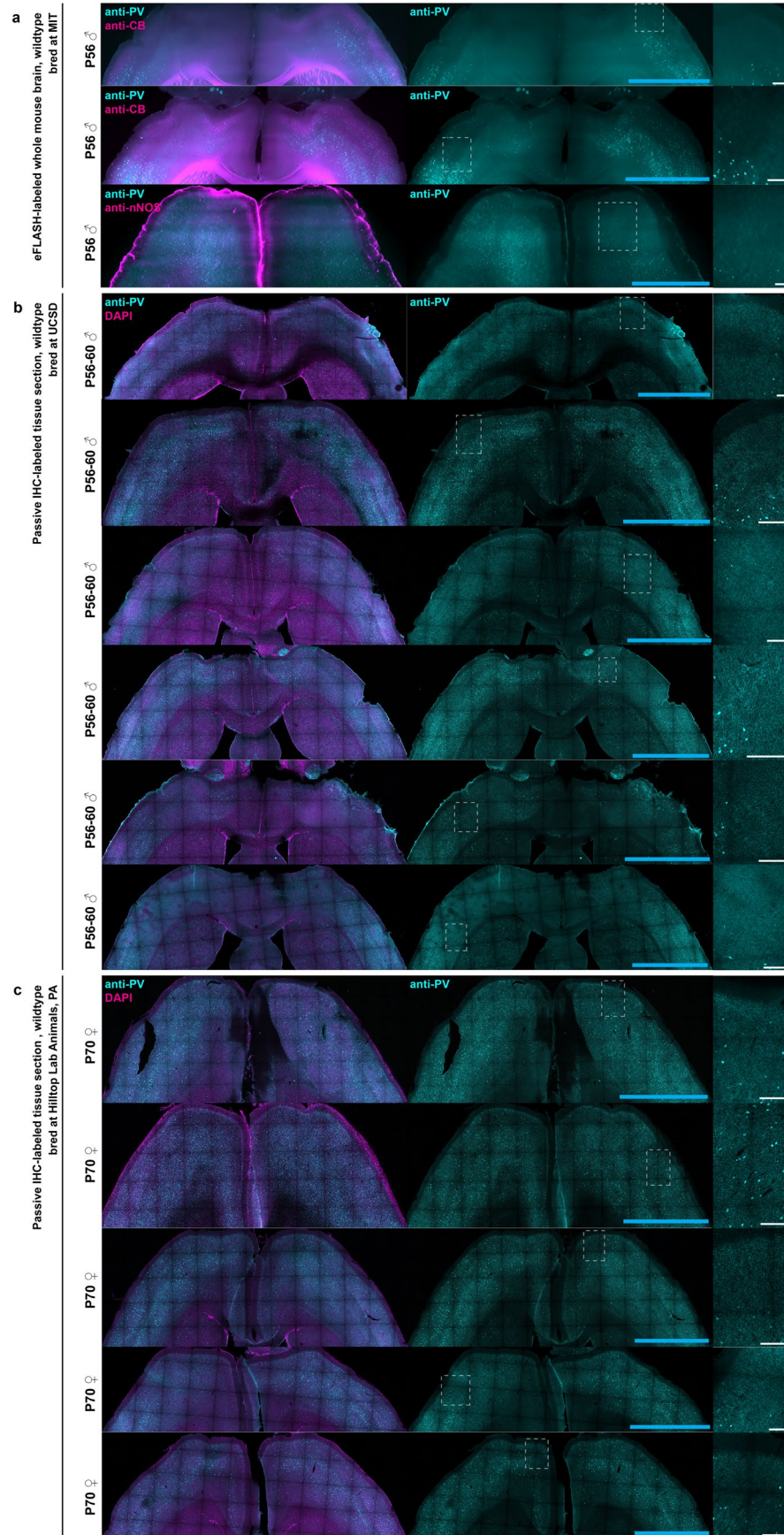


Extended Data Fig. 5 | See next page for caption.

Extended Data Fig. 5 | Quantitative brain-wide cell type mapping.

(a) Representative optical section images of intact mouse hemispheres immunolabeled using eFLASH. Automatically detected cell center coordinates are overlaid as red dots. (b) Magnified images of a. (c) Representative coronal plane heatmaps of 3D cell type density data. (d) Representative optical section image of dual immunolabeling using eFLASH. Anti-NPY (yellow) and anti-SST (magenta) co-positive cell center coordinates are overlaid with red dots.

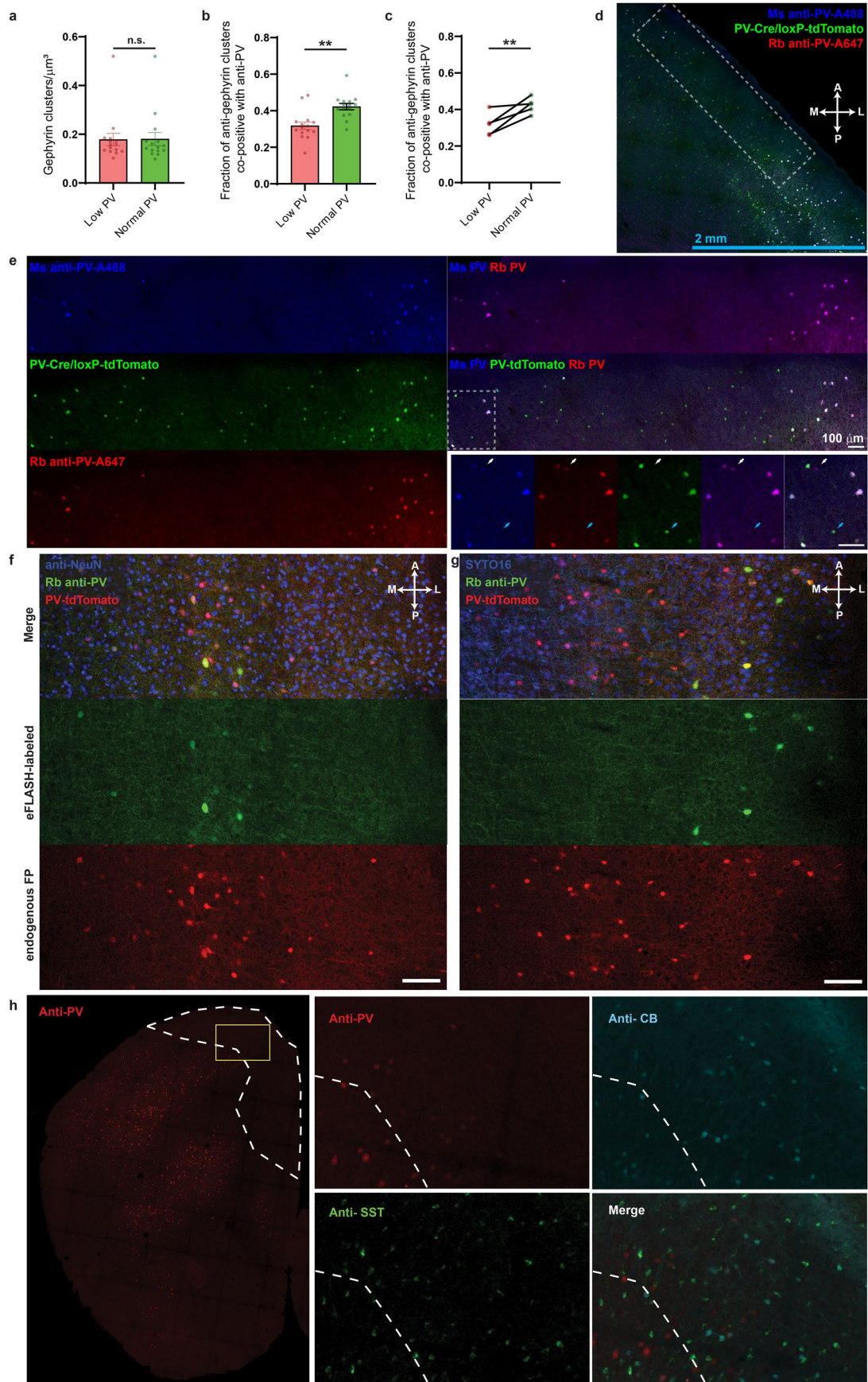
(e) Magnified images of d. (f) Representative coronal plane heatmaps of the 3D NPY/SST co-positivity data. (g) Representative optical section image of anti-c-Fos immunolabeling using eFLASH. The mouse experienced contextual fear conditioning 90 minutes before sacrifice. (h) Magnified images of g. (i) Representative coronal plane heatmaps of the c-Fos+ cell density data. Scale bars = 2 mm (cyan) and 20 mm (white).



Extended Data Fig. 6 | See next page for caption.

Extended Data Fig. 6 | Large-scale regionalized loss of anti-PV+ cells in prefrontal cortex of adult wildtype mice. (a) Adult (P56) male whole mouse brains labeled with anti-PV (cyan) and anti-CB or anti-nNOS (magenta) using eFLASH. Observed with low-PV zones (LPZs). Representative optical sections (horizontal plane) and magnified images of regions marked with dotted boxes. 20 mm MIP. Mice bred at MIT facility. All replicates shown, 3 animals. (b-c) Randomly chosen 11 mouse brains sourced from (b) UCSD and (c) Hilltop

Lab Animals (Scottsdale, PA). 200 μ m-thick horizontal mouse brain sections passively immunolabeled with anti-PV (cyan) and DAPI (magenta). (b) 20-40 mm MIP images from 6 adult (8 weeks old) male mice samples. (c) 20-40 mm MIP images from 5 adult (10 weeks old) female mice samples. Dotted box regions are chosen to highlight low anti-PV cell density regions if present. Scale bars = 2 mm (cyan) and 200 μ m (white).



Extended Data Fig. 7 | See next page for caption.

Extended Data Fig. 7 | Validation of low PV soma density regions.

(a-c) Quantification of gephyrin clusters in low PV (red bars) and normal regions (green bars). (a) Density of Gephyrin clusters. (b-c) Fraction of gephyrin clusters co-positive with anti-PV, averaged in each ROI (b) and in each brain section (c). $N = 5$ animals. 3 ROIs each for low PV and normal regions per animal. One-Way ANOVA, n.s. = not significant, $**P = 0.0013$. Mean \pm s.e.m. (d-e) Double passive immunolabeling of PV-Cre/*loxP*-tdTomato (green) mouse horizontal section with rabbit-host anti-PV (red) and mouse-host anti-PV (blue). (e) Magnified images

from the marked box in d. In the inset, MsPV+/RbPV+/tdTomato- cell (white arrow) and MsPV-/RbPV-/tdTomato+ cell (cyan arrow). (f-g) Horizontal brain sections from PV-Cre/*loxP*-tdTomato (red) double transgenic mice eFLASH-immunolabeled with anti-PV (green) with additional round of passive labeling: (f) anti-NeuN (blue) and (g) SYTO16 (blue). d-g Representative images from 3 animals. (h) Passive immunolabeling of anti-PV (red), anti-CB (cyan), and anti-SST (green). Low PV region delineated with dotted white boundary. Scale bars = 2 mm (cyan) and 100 μ m (white). $N = 1$ animal.

Reporting Summary

Nature Portfolio wishes to improve the reproducibility of the work that we publish. This form provides structure for consistency and transparency in reporting. For further information on Nature Portfolio policies, see our [Editorial Policies](#) and the [Editorial Policy Checklist](#).

Statistics

For all statistical analyses, confirm that the following items are present in the figure legend, table legend, main text, or Methods section.

- | | |
|-------------------------------------|--|
| n/a | Confirmed |
| <input type="checkbox"/> | <input checked="" type="checkbox"/> The exact sample size (n) for each experimental group/condition, given as a discrete number and unit of measurement |
| <input type="checkbox"/> | <input checked="" type="checkbox"/> A statement on whether measurements were taken from distinct samples or whether the same sample was measured repeatedly |
| <input type="checkbox"/> | <input checked="" type="checkbox"/> The statistical test(s) used AND whether they are one- or two-sided
<i>Only common tests should be described solely by name; describe more complex techniques in the Methods section.</i> |
| <input checked="" type="checkbox"/> | <input type="checkbox"/> A description of all covariates tested |
| <input type="checkbox"/> | <input checked="" type="checkbox"/> A description of any assumptions or corrections, such as tests of normality and adjustment for multiple comparisons |
| <input type="checkbox"/> | <input checked="" type="checkbox"/> A full description of the statistical parameters including central tendency (e.g. means) or other basic estimates (e.g. regression coefficient) AND variation (e.g. standard deviation) or associated estimates of uncertainty (e.g. confidence intervals) |
| <input type="checkbox"/> | <input checked="" type="checkbox"/> For null hypothesis testing, the test statistic (e.g. F , t , r) with confidence intervals, effect sizes, degrees of freedom and P value noted
<i>Give P values as exact values whenever suitable.</i> |
| <input checked="" type="checkbox"/> | <input type="checkbox"/> For Bayesian analysis, information on the choice of priors and Markov chain Monte Carlo settings |
| <input checked="" type="checkbox"/> | <input type="checkbox"/> For hierarchical and complex designs, identification of the appropriate level for tests and full reporting of outcomes |
| <input checked="" type="checkbox"/> | <input type="checkbox"/> Estimates of effect sizes (e.g. Cohen's d , Pearson's r), indicating how they were calculated |

Our web collection on [statistics for biologists](#) contains articles on many of the points above.

Software and code

Policy information about [availability of computer code](#)

Data collection For fluorescent confocal microscopy imaging, LAS X software (version 3.5.5.19976) by Leica Microsystems was utilized. For fluorescent light-sheet microscopy imaging, SmartSPIM software (version 5.5.0.1) by Life Canvas Technology was utilized.

Data analysis For particle analyses on thin confocal microscopy data (cell somata in Fig. 2 or synaptic puncta in Fig 6.), ImageJ's Particle Analysis functionality was used in conjunction with its macro/batch processing tools (<https://imagej.net/imaging/particle-analysis>).

ImageJ and Imaris 9.3 by Bitplane is utilized for visualizations.

The custom code used for volumetric image processing and cell detection, which incorporates the Nuggt python package, can be found in the following public GitHub repository <https://github.com/chunglabmit/eflash>.

For manuscripts utilizing custom algorithms or software that are central to the research but not yet described in published literature, software must be made available to editors and reviewers. We strongly encourage code deposition in a community repository (e.g. GitHub). See the Nature Portfolio [guidelines for submitting code & software](#) for further information.

Data

Policy information about [availability of data](#)

All manuscripts must include a [data availability statement](#). This statement should provide the following information, where applicable:

- Accession codes, unique identifiers, or web links for publicly available datasets
- A description of any restrictions on data availability
- For clinical datasets or third party data, please ensure that the statement adheres to our [policy](#)

All data supporting the findings of this study, including computational modeling data and primary image volumes, are available from the corresponding author upon reasonable request.

Research involving human participants, their data, or biological material

Policy information about studies with [human participants or human data](#). See also policy information about [sex, gender \(identity/presentation\), and sexual orientation](#) and [race, ethnicity and racism](#).

Reporting on sex and gender	N/A
Reporting on race, ethnicity, or other socially relevant groupings	N/A
Population characteristics	N/A
Recruitment	N/A
Ethics oversight	Banked human brain tissue sample in formalin solution were obtained from Massachusetts General Hospital. The brains were collected and banked in accordance with approval from the local Institutional Review Board.

Note that full information on the approval of the study protocol must also be provided in the manuscript.

Field-specific reporting

Please select the one below that is the best fit for your research. If you are not sure, read the appropriate sections before making your selection.

Life sciences Behavioural & social sciences Ecological, evolutionary & environmental sciences

For a reference copy of the document with all sections, see [nature.com/documents/nr-reporting-summary-flat.pdf](https://www.nature.com/documents/nr-reporting-summary-flat.pdf)

Life sciences study design

All studies must disclose on these points even when the disclosure is negative.

Sample size	No statistical methods were used to predetermine sample size. Sample sizes were chosen based on the need for a feasible, brain-wide evaluation of differences in PV-immunoreactive and transgenically labeled PV cells while considering biological variability and resource constraints. Minimum sample size of five age- and sex- matched mice was chosen for holistic brain-wide evaluation of difference between the distribution of PV-immunoreactive cells and transgenically labeled PV cells with consideration of the scale of experiment and analysis. Sample size of 7 was used for this submission. For low-PV region validation in wildtype mice, five sex- and age-matched male mice (from UCSD) and six sex- and age-matched female mice (from Hilltop Lab Animals inc.) were utilized. These sample sizes are sufficient to holistically detect meaningful differences in cell distributions given the focus of the study was on identifying broad patterns that exist in nature rather than measuring statistical significance after manipulations.
Data exclusions	No data was excluded from analysis
Replication	Each whole brain labeling is an independent experiment for demonstration of the organ-scale labeling technology eFLASH. The number of independent intact tissue labeling experiments for each targets are summarized in the statistics and reproducibility section in the methods or individual figure legends where appropriate. All internal replicates of finalized whole brain immunolabeling protocols were successful. For reproducibility of observation of low-PV zones (LPZs) in healthy wildtype mice, mice were sourced from total of three different institutes throughout the United States to control for potential environmental variables (MA, PA, and CA).
Randomization	For all labeling validation experiments, animals were randomly chosen. All available mice cohort with matched age and sex were utilized for LPZ-related experiments. For all other experiments, experimental groups were not relevant as they are demonstrations of the technology rather than a comparison between experimental conditions.
Blinding	No prior screening for LPZ was performed and all available mice cohort of matched age and sex were used. Blinding was not relevant since all available cohort was used to investigate the difference between PV-tdTomato and anti-PV signal within each animal.

Reporting for specific materials, systems and methods

We require information from authors about some types of materials, experimental systems and methods used in many studies. Here, indicate whether each material, system or method listed is relevant to your study. If you are not sure if a list item applies to your research, read the appropriate section before selecting a response.

Materials & experimental systems

- n/a Involved in the study
- Antibodies
- Eukaryotic cell lines
- Palaeontology and archaeology
- Animals and other organisms
- Clinical data
- Dual use research of concern
- Plants

Methods

- n/a Involved in the study
- ChIP-seq
- Flow cytometry
- MRI-based neuroimaging

Antibodies

Antibodies used

Antibody information is tabulated in Supplementary Table 1 and Supplementary Table 2. While antibody dilutions are not directly relevant for eFLASH labeling, they can be calculated by dividing the ug of antibody used in the supplementary table with 7.5 mL.

Below are the list of the clones of the monoclonal antibodies used in this study.

anti-a-SMA Millipore C6198 clone: 1A4
 anti-c-Fos abcam ab214672 clone: EPR20769
 anti-calbindin CST 13176BF clone: D114Q
 anti-calbindin Encor MCA-4H7 clone: MCA-4H7
 anti-GFAP Biolegend 644708 clone: 2E1.E9
 anti-Histone H3 abcam ab237418 clone: E191
 anti-IBA1 CST 17198 clone: E404W
 anti-NeuN CST 24307S clone: D4G4O
 anti-Nf-M Encor MCA-3H11 clone: 3H11
 anti-NPY CST 11976S clone: D7Y5A
 anti-SST Santa Cruz sc-47706 clone: YC7
 anti-TH Biolegend 818001 clone: 2/40/15
 anti-Tubulin β 3 Biolegend 801208 clone: TUJ1
 anti-Vimentin CST 9856S clone: D21H3

Validation

Validation information for antibodies available in multiple hosts are summarized in Supplementary Figure 1. All antibody signals were compared to known distribution through prior literature and/or Allen brain ISH data. Specific antibodies and their location on main figures and extended data figures are tabulated in Supplementary Table 2.

Animals and other research organisms

Policy information about [studies involving animals](#); [ARRIVE guidelines](#) recommended for reporting animal research, and [Sex and Gender in Research](#)

Laboratory animals

For mice, C57BL/6 (wildtype), ChATBAC-eGFP (Jackson Stock No. 007902), PV-Cre / loxP-tdTomato double hemizygous (B6 Pvalb-IRES-Cre, Jackson Strain#017320 and Ai14, Jackson Strain#007914) were used. All mice collected were adults between 8 to 10 weeks (P56 ~ P70).

For rats, PFA-perfused whole brains of CVF Sprague-Dawley rat weanlings (P21 to P28) were purchased from Hilltop Lab Animals, Inc. (Scottsdale, PA).

For marmoset, one adult common marmoset (wild) was perfused by an expert at Guoping lab (MIT) following the approved protocol described in the methods.

Wild animals

No wild animals were used in this study.

Reporting on sex

Both male and female mice are included low-PV zone (LPZ) validation in wildtype animals.

Only age- and sex-matched (male) mice are included in the study of LPZ in PV-Cre/loxP-tdTomato to control for individual variability.

Field-collected samples

No field collected samples were used in this study

Ethics oversight

All animal experiments were approved by the Institutional Animal Care and Use Committee of Massachusetts Institute of Technology and were performed under the guidelines from the National Institute of Health. All animals were housed in AAALAC-accredited facilities.

Note that full information on the approval of the study protocol must also be provided in the manuscript.

Plants

Seed stocks

N/A

Novel plant genotypes

N/A

Authentication

N/A